Cell Reports
Methods

Article

Comparative analysis of CI- and CIV-containing respiratory supercomplexes at single-cell resolution

Graphical abstract

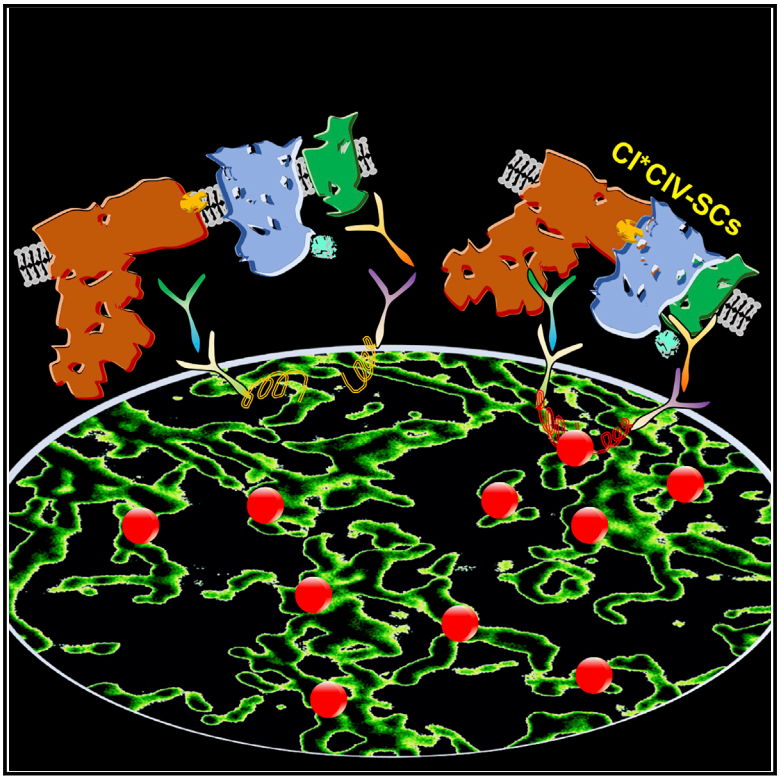

Highlights

- Inhibition of the OXPHOS system might lead to a decreased number of CI*CIV-SCs
- Single-cell CI*CIV-SC staining is feasible in fixed brain tissues
- Quantification of CI*CIV-SCs can be used for genetic and pharmacological screens
- CI*CIV-SC loss might correlate with diminished OCRs in some experimental models

Authors

Fabio Bertan, Lena Wischhof, Enzo Scifo, ..., Dan Ehninger, Pierluigi Nicotera, Daniele Bano

Correspondence

pierluigi.nicotera@dzne.de (P.N.), daniele.bano@dzne.de (D.B.)

In brief

Bertan et al. validate a proximity ligation assay-based method for single-cell comparative assessment of mitochondrial function and dysfunction. Through correlative analyses in multiple model systems, they demonstrate that the abundance of mitochondrial CI, CIV-containing respiratory supercomplexes is a suitable proxy marker to investigate mitochondrial lesions in fixed materials, including postmortem tissues.

Bertan et al., 2021, Cell Reports Methods *1*, 100002
May 24, 2021
https://doi.org/10.1016/j.crmeth.2021.100002

CellPress

Cell Reports Methods

CellPress
OPEN ACCESS

Article

Comparative analysis of CI- and CIV-containing respiratory supercomplexes at single-cell resolution

Fabio Bertan,[1] Lena Wischhof,[1] Enzo Scifo,[1] Mihaela Guranda,[1] Joshua Jackson,[1] Anaïs Marsal-Cots,[1] Antonia Piazzesi,[1] Miriam Stork,[1] Michael Peitz,[2,3] Jochen Herbert Martin Prehn,[4] Dan Ehninger,[1] Pierluigi Nicotera,[1,*] and Daniele Bano[1,5,*]

[1]German Center for Neurodegenerative Diseases (DZNE), Deutsches Zentrum für Neurodegenerative Erkrankungen (DZNE), Venusberg-Campus 1, Gebäude 99, Bonn, North Rhine-Westphalia 53127, Germany

[2]Institute of Reconstructive Neurobiology, University of Bonn Medical Faculty and University Hospital Bonn, Bonn, North Rhine-Westphalia 53127, Germany

[3]Cell Programming Core Facility, University of Bonn Medical Faculty, Bonn, North Rhine-Westphalia 53127, Germany

[4]Royal College of Surgeons in Ireland, Department of Physiology and Medical Physics Department, D02 YN77 Dublin, Ireland

[5]Lead contact

*Correspondence: pierluigi.nicotera@dzne.de (P.N.), daniele.bano@dzne.de (D.B.)

https://doi.org/10.1016/j.crmeth.2021.100002

MOTIVATION The detection of mitochondrial lesions in patient-derived tissues represents a powerful diagnostic tool. However, in complex organs, such as the brain, neurodegenerative processes often alter the cell composition of the tissue, with extensive microgliosis influencing population-based analyses of mitochondrial bioenergetics. To detect cell-type-specific mitochondrial lesions in tissues, we developed a PLA-based method in which complex I, complex IV-containing mitochondrial supercomplexes (CI*CIV-SCs) can be visualized as dot-like structures. This assay may be an alternative and complementary approach for the detection of mitochondrial perturbation in fixed materials.

SUMMARY

Mitochondria sustain the energy demand of the cell. The composition and functional state of the mitochondrial oxidative phosphorylation system are informative indicators of organelle bioenergetic capacity. Here, we describe a highly sensitive and reproducible method for a single-cell quantification of mitochondrial CI- and CIV-containing respiratory supercomplexes (CI*CIV-SCs) as an alternative means of assessing mitochondrial respiratory chain integrity. We apply a proximity ligation assay (PLA) and stain CI*CIV-SCs in fixed human and mouse brains, tumorigenic cells, induced pluripotent stem cells (iPSCs) and iPSC-derived neural precursor cells (NPCs), and neurons. Spatial visualization of CI*CIV-SCs enables the detection of mitochondrial lesions in various experimental models, including complex tissues undergoing degenerative processes. We report that comparative assessments of CI*CIV-SCs facilitate the quantitative profiling of even subtle mitochondrial variations by overcoming the confounding effects that mixed cell populations have on other measurements. Together, our PLA-based analysis of CI*CIV-SCs is a sensitive and complementary technique for detecting cell-type-specific mitochondrial perturbations in fixed materials.

INTRODUCTION

Mitochondria are double-membrane organelles that supply ATP and essential building molecules for cell growth, maintenance, and division. In differentiated cells under normal aerobic conditions, oxidative phosphorylation (OXPHOS) accounts for approximately 90% of the total required cellular energy (Wallace, 2018). Three complexes (i.e., CI, CIII, and CIV) of the OXPHOS system couple the electron transfer to proton translocation across the inner mitochondrial membrane, thereby creating an electrochemical gradient that the ATP synthase (or complex V) utilizes for ATP production. Although individual respiratory complexes can randomly diffuse and transiently interact (Hackenbrock et al., 1986), they can also associate in stable, higher-order structures in equilibrium within the inner membrane of the cristae. It has been suggested that these "supercomplexes" (Schagger and Pfeiffer, 2000) might promote assembly and stability, kinetic advantages, and functional flexibility of proton-pumping complexes (Lapuente-Brun et al., 2013; Acin-Perez et al., 2008; Letts et al., 2019; Wu et al., 2016; Garcia-Poyatos et al., 2020; Calvo et al., 2020; Berndtsson et al., 2020; Moreno-Lastres et al., 2012; Schagger et al., 2004). Although the physiological role remains a topic of intense scientific debate, it appears that superassembled complexes can enhance

respiratory capacity and, as a consequence, limit the formation of by-products, such as reactive oxygen species (ROS) (Maranzana et al., 2013; Lapuente-Brun et al., 2013; Calvo et al., 2020; Lopez-Fabuel et al., 2016). Less clear is whether these higher-order respiratory supercomplexes (RSCs) enable a more efficient electron transfer and substrate channeling function (Letts et al., 2019; Lapuente-Brun et al., 2013; Bianchi et al., 2004; Fedor and Hirst, 2018; Calvo et al., 2020; Blaza et al., 2014). In terms of organization, the CIV-containing NADH-respirasome (or I-III_2-IV-RSC or simply N-respirasome) is an assembly as large as 19 nm in height and 30 nm in length (Letts et al., 2016; Gu et al., 2016; Guo et al., 2017), and consists of fully assembled CI, CIII, and CIV in a ratio of 1:2:1 (Schagger and Pfeiffer, 2001; Calvo et al., 2020). The remaining fractions of CI and CIV can also organize in alternative assemblies with CIII, further expanding the array of possible quaternary species (Lapuente-Brun et al., 2013; Cogliati et al., 2016; Letts et al., 2019; Calvo et al., 2020; Schagger and Pfeiffer, 2000, 2001; Protasoni et al., 2020; Lobo-Jarne et al., 2020). On the basis of recent evidence, $CIII_2$ is central for both electron transport chain (ETC) homeostasis and RSC biogenesis, given that it recruits components of nascent CI and CIV and acts as a primary seed that positively stimulates the full assembly and stability of individual complexes (Protasoni et al., 2020; Calvaruso et al., 2012). As originally postulated (Schagger and Pfeiffer, 2000), the presence and ratio of different RSCs depend on various factors (e.g., background, polymorphism, epigenetic regulation of gene expression) as well as tissue composition and bioenergetic demands of individual cells (Sun et al., 2016; Lapuente-Brun et al., 2013; Cogliati et al., 2016; Calvo et al., 2020; Mourier et al., 2014; Greggio et al., 2017). Functional defects, environmental toxins, and genetic lesions that impair the expression and incorporation of ETC components can irremediably undermine the proper formation of respiratory complexes and, as a consequence, of functional respirasomes (Acin-Perez et al., 2008; Protasoni et al., 2020; Cogliati et al., 2016; Lapuente-Brun et al., 2013; Calvo et al., 2020; Lobo-Jarne et al., 2020). Given that aberrant mitochondrial bioenergetics often lead to metabolic syndromes, inherited pathologies, and debilitating neurodegenerative diseases (Bano and Prehn, 2018; Frazier et al., 2019; Gorman et al., 2016; Area-Gomez and Schon, 2014), the assessment of RSCs in patient-derived materials might provide additional informative cues about disease etiology.

In biomedicine, a range of cellular parameters have been used as proxy markers to assess mitochondrial function and/or lesions (Connolly et al., 2018; Frazier et al., 2020). In the last 2 decades, innovative approaches have been developed for population-based quantifications of mitochondrial bioenergetics, of which one prevailing functional readout is the amount of O_2 consumed over time. The most advanced systems measure oxygen consumption rate (OCR) using conventional O_2 electrode chambers (e.g., Hansatech Oxygraph), O_2-sensitive fluorescent indicators (e.g., Seahorse XF flux analyzer, Luxcel Bioscience's MitoXpress), and amperometric O_2 sensors (e.g., Oroboros Oxygraph-2k system) (Connolly et al., 2018). Despite the robustness and reliability of OCR measurements, these methods show several limitations in cell-specific assessment of mitochondrial performance in complex tissues such as the brain, unless laborious cell sorting precedes any analysis. To overcome this drawback, time-lapse fluorescence imaging analysis of various mitochondrial parameters (e.g., membrane potential, ROS, Ca^{2+} signaling, *in situ* respiration) can effectively be performed in living tissues, as long as cell-type-specific labeling (e.g., overexpression of a fluorescent protein as a marker) is available. Because none of these methods can be applied to fixed materials, one standard and widely accepted approach involves stainings of distinct ETC subunits in combination with markers that allow for discrimination of probe signals in a cell-type-specific manner. The sequential analysis using selected and properly validated antibodies against subunits of the five OXPHOS complexes can enable the quantification of eventual changes in mitochondrial activity. Although this method is sufficiently accurate in the case of mitochondrial lesions associated with human pathologies (Wallace, 2018; Lake et al., 2016), it becomes less adequate to quantitatively measure adjustments because of biological processes that require the fine-tuning of mitochondrial respiration, as in the case of cell differentiation or tumor formation. Similarly, this approach has limitations when OXPHOS assembly intermediates are still present in cells carrying lesions of unknown nature or upon exposure to toxins that interfere with mitochondrial biology. Other technical drawbacks include intrinsic experimental variability (i.e., instrument setup and imaging acquisition parameters, sample collection, and preparation) and eventual age-dependent accumulation of endogenous pigments (e.g., melanin) and lipochromes (e.g., lipofuscin) that might enhance autofluorescence background. Thus, a reliable *in situ* assessment of mitochondrial respiratory integrity in freshly prepared patient-derived samples or postmortem tissues still remains technically challenging, undermining diagnostic analyses as well as biomedical studies.

Starting with the knowledge that components of the OXPHOS system can associate in higher-order structures (Cogliati et al., 2016; Lapuente-Brun et al., 2013; Schagger and Pfeiffer, 2000; Calvo et al., 2020), we hypothesized that the abundance of RSCs might correlate with the integrity of the OXPHOS system and would sufficiently depict the state of mitochondrial function/dysfunction. Given that the length of the mammalian CIV-containing NADH-respirasomes (i.e., I_1+III_2+IV_1) is approximately 30 nm (Wu et al., 2016) and, therefore, within the detectable range of a proximity ligation assay (PLA) (Fredriksson et al., 2002), we set out to develop an image-based protocol for measuring the abundance of CI- and CIV-containing superassembled structures (hereafter referred to as CI*CIV-SCs) at single-cell resolution. We herein present our optimized, widely accessible, and highly sensitive method that quantitatively profiles the state of the mitochondrial respiratory chain in fixed tissues.

RESULTS

Proximity ligation-based staining allows the detection of mitochondrial CI*CIV-SCs in fixed cells

We set off to design a reproducible and widely applicable proximity ligation-based method for visualizing and quantifying CI*-CIV-SCs at single-cell resolution (Figure 1A). Because most of the stimulated emission depletion (STED) microscopes can

CellPress
OPEN ACCESS

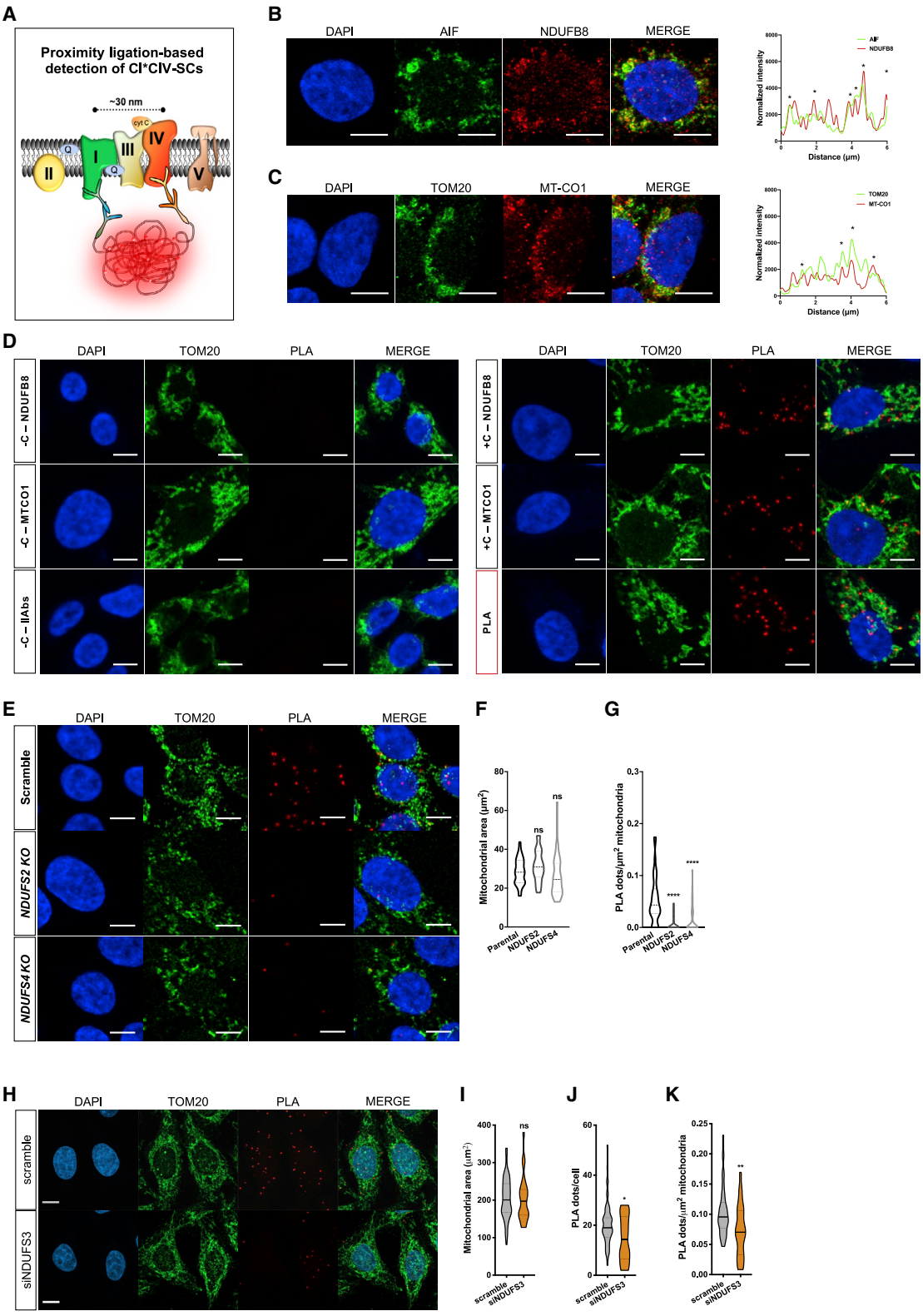

Figure 1. CI*CIV-SCs are detectable in fixed cultured cells using PLA staining

(A) Scheme of the PLA-based approach to visualize CI*CIV-SCs. Primary antibodies against nuclear-encoded CI subunit NDUFB8 and mitochondrial DNA-encoded CIV subunit MTCO1 are used to detect superassembled structures.

(legend continued on next page)

accommodate only two channels in the STED mode, and because depletion lasers would be within the excitation wavelength of most commercially available PLA probes, we developed our protocol with an Airyscan confocal microscope with a resolution between 120 and 140 nm. We selected NADH dehydrogenase [ubiquinone] 1β subcomplex subunit 8 (NDUFB8) and cytochrome *c* oxidase subunit I (COX1 or MTCO1) because of their ubiquitous expression profiles across tissues (Calvo et al., 2016; Pagliarini et al., 2008). Primary antibodies against NDUFB8 and MTCO1 were chosen on the basis of their different immunoglobulins G (IgGs) (rabbit and mouse), high specificity, and prior experimental validation in some of our works (Troulinaki et al., 2018; Wischhof et al., 2018; Meyer et al., 2015). As an initial cellular model, we employed near-haploid tumorigenic HAP1 cells. High-resolution Airyscan confocal imaging analysis of NDUFB8 and MTCO1 revealed a clear colocalization with mitochondrial AIF and TOM20, respectively (Figures 1B and 1C). We validated our PLA conditions by using different positive and negative controls (Figure 1D). In this regard, we observed signal when each primary antibody (i.e., NDUFB8 and MTCO1) was individually incubated with two oligonucleotide-labeled secondary antibodies that recognized the same IgG (Figure 1D, positive controls, +C). Conversely, no signal was observed in cells incubated with only one primary antibody and secondary antibodies against different IgGs or when the two secondary antibodies were incubated without primary antibodies (Figure 1D, negative controls, −C). When PLA was carried out using both anti-NDUFB8 and anti-MTCO1 antibodies together with their corresponding species-specific secondary antibodies, fluorescence-positive PLA dot-like structures were easily detectable, clearly quantifiable, and primarily colocalized within mitochondrial TOM20-labeled structures (Figure 1D) (for more details, please see STAR Methods). Having established the optimal experimental conditions for our assay, we tested whether our method could detect changes in mitochondrial RSCs by using cells carrying genetic lesions of the OXPHOS system. Because CI mutations inhibit the formation of CI*CIV-SCs, as previously described (Calvo et al., 2020), we quantified variations of CI*-CIV-SC content in *NDUFS2* and *NDUFS4* knockout (KO) HAP1 cells, with both tumorigenic cell lines having defective mitochondrial respiration (Gioran et al., 2019). We found that, although the TOM20-labeled mitochondrial network did not reveal obvious differences (Figures 1E and 1F), there were significantly fewer PLA dots in KO cells compared with parental controls (Figures 1E and 1G). To corroborate our findings in another cellular system, we transfected HeLa cells with scramble and small interfering RNA (siRNA) against *NDUFS3*. Compared with control, we found that transient downregulation of the CI subunit NDUFS3 did not alter mitochondrial area, whereas it decreased the number of PLA dots (Figures 1H–1K). Together, this first set of validation data indicate that our proximity ligation-based staining is sufficiently sensitive to detect differences in CI*CIV-SCs in mitochondria-deficient cells.

CI*CIV-SC content diminishes in the brain of a mouse model of Leigh syndrome

We sought to evaluate the versatility of our PLA-based method in defining mitochondrial defects in neurons of brain tissues. To do so, we employed control (i.e., wild type [WT]) and *Ndufs4* KO mice, the latter being a widely accepted preclinical model of Leigh syndrome (Quintana et al., 2010; Kruse et al., 2008). As previously shown, *Ndufs4* KO mice exhibit clear signatures of aberrant OXPHOS causally linked to the development of encephalomyopathy, ultimately resulting in premature death within 7–10 weeks of age (Quintana et al., 2010; Kruse et al., 2008). First, we measured OCR in *ex vivo* brain slices from 1-month-old control and *Ndufs4* KO mice, where we observed a tendency toward decreased basal respiration and response to mitochondrial inhibitors compared with controls (Figure 2A). Then, we separated proteins by using conventional sodium dodecyl sulfate polyacrylamide gel electrophoresis (SDS-PAGE) and performed immunoblot analyses. As expected, we observed a severe CI deficiency in samples from *Ndufs4* KO mice (Figure 2B). When we tested the loss of RSCs by using blue native (BN)-PAGE and subsequent immunoblot analysis of whole-brain lysates, we found a reduction of RSCs and a consequent increased amount of superassembled structures at lower molecular weights (Figure 2C). After validation and optimization of our antibodies in fixed brain tissues (Figures 2D and 2E), we ran high-resolution Airyscan confocal microscopy and 3D rendering of double immunofluorescence staining, with PLA signals that colocalized with mitochondrial TOM20-labeled structures in neurons (Figure 2F). We carried out imaging analyses of hippocampal sections from age-matched *Ndufs4* KO mice and control littermates. PLA-based visualization of CI*CIV-SCs was performed along with immunostaining of the neuronal marker NeuN and the mitochondrial marker TOM20 (Figures 2G and 2H). High-resolution confocal microscopy and 3D rendering of confocal stacks revealed that WT and *Ndufs4* KO CA1 neurons had comparable somatic sizes (Figure 2I). However, KO cells exhibited a smaller mitochondrial network (Figure 2J) with a mitochondria-to-soma ratio that was statistically different from that of control neurons (Figure 2K). When normalized to the cell body or to mitochondrial area, the number of PLA dots was

(B and C) Immunostaining and fluorescence profile of (B) AIF (green) and NDUFB8 (red) and (C) TOM20 (green) and MTCO1 (red) in parental HAP1 cells (scale bar, 5 μm). Colocalization analyses are reported on the right (stars show the overlapping fluorescent signals relative to distance).

(D) PLA-based detection of CI*CIV-SCs (red dots) along with staining of the mitochondrial marker TOM20 (green) and the nuclear marker DAPI (blue). Negative and positive experimental controls are reported for NDUFB8, MTCO1, and respective secondary IgGs in HAP1 cells. Scale bar, 5 μm.

(E) Representative confocal images of parental, *NDUFS2* KO, and *NDUFS4* KO HAP1 cells stained with DAPI (nucleus, blue), TOM20 (mitochondria, green), and PLA (CI*CIV-SCs, red). Scale bar, 5 μm.

(F and G) Quantification of (F) mitochondrial area and (G) CI*CIV-SCs normalized to mitochondrial area (n = 3, parental = 37 cells, *NDUFS2* KO = 22 cells, *NDUFS4* KO = 37 cells, one-way ANOVA, ****$p < 0.0001$, ns, not significant).

(H–K) Shown are (H) representative images and quantification of (I) mitochondrial area (μm^2), (J) PLA dots per cell, and (K) PLA dots per μm^2 mitochondria in HeLa cells transfected with scramble and siRNA against *NDUFS3* (n = 1, scramble = 60 cells, siNDUFS3 = 24 cells, Student's t test, **$p < 0.01$, *$p < 0.05$; ns, not significant). Scale bar, 10 μm.

CellPress
OPEN ACCESS

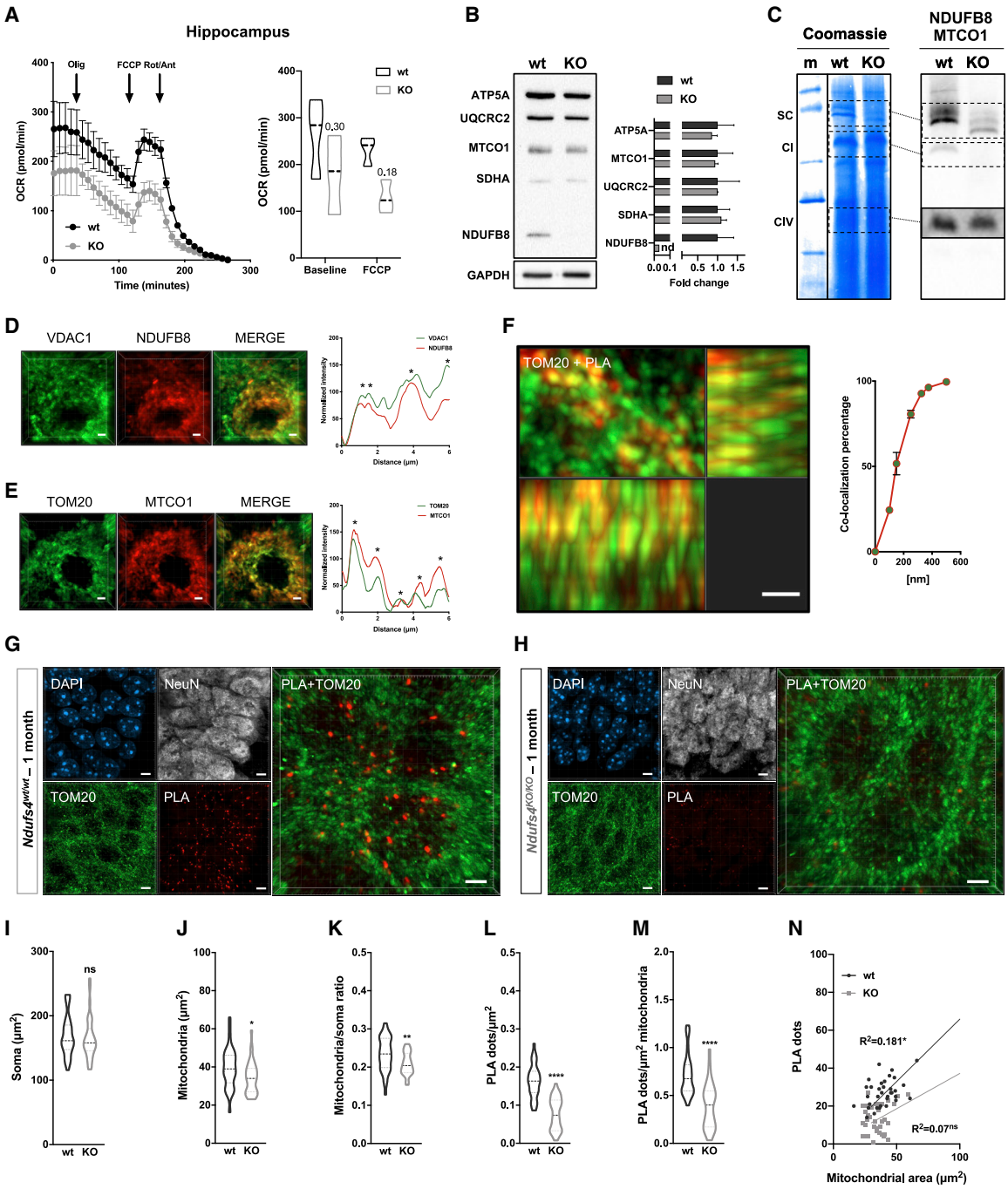

Figure 2. CI*CIV-SC content diminishes in the brain of *Ndusf4* KO mice

(A) OCR measurement in *ex vivo* hippocampal brain sections from control (WT) and *Ndufs4* knockout mice (KO) (WT, n = 3; *Ndufs4* KO, n = 3, two-way RM ANOVA). In the violin plot, numbers represent p values.

(B) Immunoblot analysis of samples from WT and KO mice using antibodies against ETC subunits (CI, NDUFB8; CII, SDHA; CIII, UQCRC2; CIV, MTCO1; CV, ATP5A; WT, n = 2; *Ndufs4* KO, n = 2). GAPDH was used as loading control. Densitometry is relative to WT samples and reported as mean ± SEM (nd, not determined).

(C) BN-PAGE and composite image of immunoblots obtained using antibodies against NDUFB8 (CI) and MTCO1 (CIV, cropped bands). Samples were from WT and KO brain homogenates (WT, n = 3; *Ndufs4* KO, n = 3).

(D and E) Coimmunostaining and fluorescence profiles of (D) VDAC1 and NDUFB8 and (E) TOM20 and MTCO1 in control mouse brain sections (two-way ANOVA, *p < 0.05). Scale bar, 5 μm.

(F) Colocalization between mitochondria (TOM20) and CI*CIV-SCs (PLA). Scale bar, 1 μm.

(legend continued on next page)

reduced by approximately half in *Ndufs4* KO CA1 neurons compared with control cells (Figures 2L and 2M). Linear correlation between PLA dots and mitochondrial area was observed only in control pyramidal cells, which was lost in *Ndufs4* KO CA1 neurons (Figure 2N). Together, our findings indicate that *Ndufs4* KO neurons have a considerable loss of CI*CIV-SCs compared with controls. Furthermore, our validated PLA-based method can quantify CI*CIV-SC content at the single-cell resolution in fixed brain sections.

Single-cell quantification of CI*CIV-SCs enables comparative assessments of mitochondrial lesions during neurodegenerative processes

To perform comparative analysis of mitochondrial lesions in brains with distinct pathological profiles, we employed two additional mouse models of mitochondrial disease. Namely, we used Harlequin (Hq) mutant mice carrying a proviral insertion in the X-linked *Aifm1* gene (Wischhof et al., 2018; Benit et al., 2008; Klein et al., 2002) and *Aifm1* (*R200 del*) knockin (KI) mice expressing a disease-associated variant of the apoptosis-inducing factor (AIF) (Wischhof et al., 2018). These two mouse models exhibit signatures of aberrant OXPHOS (Wischhof et al., 2018); however, only Hq mutant mice display obvious gliosis and loss of cerebellar Purkinje cells at 6 months of age (Figure S1A) (Wischhof et al., 2018; Klein et al., 2002). Because the Hq strain has a mixed genetic background (i.e., CBA/CaJ and C57BL/6J) (Klein et al., 2002), all analyses were strictly performed with the relative littermates. As a first step, we measured mitochondrial respiration in *ex vivo* brain sections (i.e., cerebella, hippocampi, and cortices) by using conventional Seahorse respirometry. Starting from comparable basal respiration levels, addition of mitochondrial respiratory inhibitors (i.e., oligomycin, FCCP, and rotenone and antimycin A) resulted in similar responses, with only a minor tendency toward reduced OCR in AIF-deficient tissues compared with controls (Figures S1B–S1D). Using freshly prepared brain homogenates from Hq mutant, *Aifm1* (*R200 del*) KI, and control littermates, we performed SDS-PAGE and immunoblot analyses of OXPHOS components (Figures 3A, S1E, and S1F). In line with our previous findings (Wischhof et al., 2018), we confirmed the loss of CI and CIII subunits in Hq mutant cerebella compared with controls, whereas only a moderate impairment of CI was observed in *Aifm1* (*R200 del*) KI tissues (Figures 3A, S1E, and S1F). In complex organs consisting of different cell types such as the brain, this set of data points out a technical limitation of OCR measurements in detecting mitochondrial defects associated with neurodegenerative processes.

To ensure that AIF deficiency affects RSCs, brain homogenates were loaded on N-PAGE, blue Coomassie stained, and then immunoblotted against anti-CI and anti-CIV antibodies (Figures 3B, S1G, and S1H). We ascertained a consistent reduction of RSC content in AIF-deficient cerebella relative to controls (Figure 3B). After a thorough validation of our antibodies and PLA protocol in cerebellum slices (Figures S2A–S2C), we went on to quantify CI*CIV-SCs at the single-cell level. We applied our PLA protocol on cerebellum slices from 6-month-old Hq mutant, *Aifm1* (*R200 del*) KI, and relative littermates, and then performed high-resolution confocal microscopy on calbindin-positive, TOM20-positive Purkinje neurons (Figures 3C, 3D, 3K, and 3L). As a correlative observation, in Hq mutant cerebella we noticed an evident PLA signal from cells surrounding Purkinje neurons (Figures 3C and 3D), which is probably due to the large number of microglial cells in the degenerating tissue, as previously reported (Wischhof et al., 2018; Klein et al., 2002). We performed a detailed quantification of mitochondrial area and CI*-CIV-SCs in calbindin-positive cells (Figures 3C, 3D, 3K, and 3L). Compared with cells from control tissues, AIF-deficient neurons had reduced soma size and mitochondrial area (Figures 3E, 3F, 3M, and 3N), possibly more pronounced in KI cells, given that the mitochondria-to-soma ratio was statistically different from controls (Figures 3G and 3O). Importantly, PLA-based quantification (normalized to the area of the soma) revealed that CI*-CIV-SCs were diminished by 57% (Figure 3H) and 62.5% (Figure 3P) in Hq and *Aifm1* (*R200 del*) KI Purkinje neurons, respectively, compared with controls. When PLA dots were normalized to the mitochondrial area, CI*CIV-SC content was decreased by 46.9% in Hq cells (Figure 3I) and by 57.8% in *Aifm1* (*R200 del*) KI cells (Figure 3Q) compared with control neurons. A linear correlation between PLA dots and the mitochondrial area was observed only in tissues from C57BL/6NTac mice (Figures 3J and 3R), further emphasizing the contribution of the genetic background to RSC content as previously described (Cogliati et al., 2016; Calvo et al., 2020). Despite this intrinsic variability, our statistical analysis indicated that *Aifm1* (*R200 del*) KI and, even more, Hq Purkinje cells display higher heterogeneity in terms of CI*CIV-SCs, with a subpopulation of neurons that have almost no detectable superassembled structures. In summary, our findings indicate that *in situ* quantification of CI*CIV-SCs is an informative and sensitive approach for comparative analyses of mitochondrial defects in tissues undergoing neurodegenerative processes.

Enhanced RSC content is associated with stem cell differentiation and survival

Because mitochondrial bioenergetics and its rewiring significantly influence stemness, cell lineage commitment, and differentiation (Lisowski et al., 2018; Katajisto et al., 2015), we decided to compare RSCs in induced pluripotent stem cells (iPSCs) and iPSC-derived small-molecule neural precursor cells (smNPCs). We profiled their OCR upon sequential addition of mitochondrial respiratory inhibitors (Figure 4A) and found that smNPCs had a much higher spare respiratory capacity, though reduced basal

(G and H) Representative pictures of hippocampal CA1 pyramidal neurons from (G) WT and (H) KO mice stained with DAPI (nucleus), NeuN (neurons), TOM20 (mitochondria), and PLA (CI*CIV-SCs). Scale bar, 5 μm.

(I–N) Quantification of (I) area of the soma, (J) mitochondrial area, (K) mitochondria/soma ratio, (L) PLA dots normalized to the soma, (M) PLA quantification of CI*CIV-SCs normalized to the mitochondrial area, and (N) linear correlation of PLA dots and mitochondrial area (WT, n = 3, 34 cells; *Ndufs4* KO, n = 3, 37 cells). Data are represented as a violin plot with median (25th and 75th percentile), Student's t test, n = 3, ****$p < 0.0001$, **$p < 0.01$, *$p < 0.05$, ns, not significant. In (N) Linear correlation of PLA dots and mitochondrial area (WT, n = 3, 34 cells; *Ndufs4* KO, n = 3, 37 cells). Linear regression, *$p < 0.05$; ns = not significant.

CellPress
OPEN ACCESS

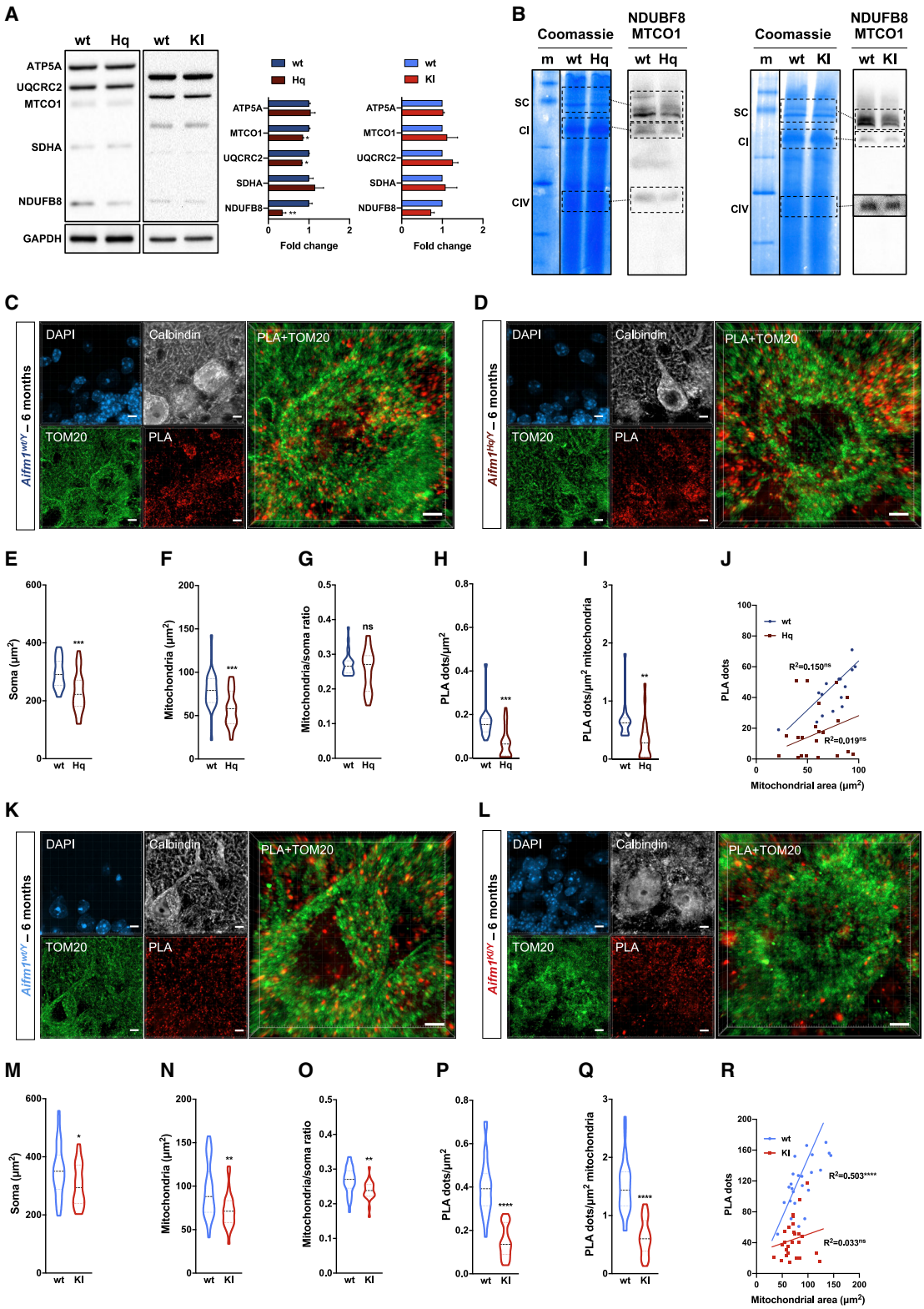

Figure 3. Single-cell quantification of CI*CIV-SCs in Purkinje cells of Hq mutant and *Aifm1* (*R200 del*) KI mice

(A) Immunoblot analysis of freshly frozen cerebella (WT, n = 3; Hq, n = 3; WT, n = 3; KI, n = 3) using antibodies against NDUFB8, SDHB, UQCRC2, MTCO1, and ATP5A. GAPDH was used as loading control. Densitometry is relative to WT samples and reported as mean ± SEM, Student's t test, *p < 0.05, **p < 0.01.

(legend continued on next page)

OCR, compared with iPSCs (Figures 4B and 4C). These differences in mitochondrial respiration were associated with variations in the composition of the OXPHOS system, including a 2-fold increase of the CIII subunit UQCRC2 and a slightly decreased expression of the CIV subunit MTCO1 (Figure 4D). BN-PAGE and subsequent immunoblots revealed a much higher content of RSCs in smNPCs compared with iPSCs (Figure 4E). We applied our PLA-based method and found that CI*CIV-SCs were much more abundant in smNPCs compared with iPSCs (Figures 4F–4G), although their number varied substantially in individual cells, possibly because of the mixed population of cells at different cell-cycle stages. Together, this line of evidence indicates that loss of stemness and consequent cell lineage commitment are linked to an evident remodeling of the OXPHOS system, with an enhanced formation of CI*CIV-SCs.

We wondered whether mitochondrial lesions would alter RSC formation in iPSCs and iPSC-derived cells. To test whether our technique could detect stalled RSC intermediates, we generated *NDUFS4* KO iPSCs by using CRISPR-Cas9 gene editing. We obtained two independent lines (indicated as KO_1 and KO_2) that carried a homozygous single-nucleotide deletion, with a consequent frameshift mutation leading to a premature stop codon (Figures S3A and S3B). Compared with control, NDUFS4 loss led to a mild decrease of basal respiration and a much lower mitochondrial respiratory capacity (Figures 4H and 4I), although only minor expression changes of other ETC subunits were detected (Figure 4J). When we ran BN-PAGE with freshly prepared samples, we detected superassembled species at lower molecular weight in *NDUFS4* KO cells compared with parental ones (Figure 4K). Using our PLA-based method, we quantified the abundance of CI*CIV-SCs and, in line with the increased amount of superassembled species in the BN-PAGE (Figure 4K), found a significant increase of PLA dots/μm^2 of mitochondria in *NDUFS4* KO iPSCs compared with parental ones (Figures 4L and 4M). A possible explanation of this observation is that the incorporation of NDUFS4 in partially superassembled CI occurs at a later stage and is necessary for the stability and optimal functionality of respirasomes as previously shown (Calvaruso et al., 2012; Mimaki et al., 2012; Moreno-Lastres et al., 2012). To further understand the impact of *NDUFS4* KO on CI*CIV-SCs, we differentiated iPSCs into cortical excitatory neurons by using transcription factor-mediated forward programming (Peitz et al., 2020). Although *NDUFS4* KO did not alter iPSC proliferation (data not shown), it severely undermined the survival of immature cortical neurons, with many cells undergoing degeneration and death (Figure 4L). We performed immunostaining of 6-day-old neurons and found that NDUFS4 KO impaired the formation of CI*-CIV-SCs in immature cortical neurons (Figures 4L and 4M). Thus, although *in situ* CI*CIV-SC assessment is a valuable proxy marker to detect and quantify mitochondrial lesions in comparative measurements across samples, our data in KO iPSCs emphasize that caution is necessary when conclusions are not corroborated by multiple complementary analyses or when the biological nature of the mitochondrial defect is unknown.

Single-cell quantification of CI*CIV-SCs is suitable for imaging-based screens

To determine whether our method can be adapted to imaging-based screens, we performed proof-of-principle experiments by using different cultured cellular models. First, we generated murine neural progenitor cells (NPCs) from adult male mice carrying an *Aifm1* allele flanked by attP/attB sites (Wischhof et al., 2018). Upon PhiC31 overexpression and homologous recombination, we genetically deleted the *Aifm1* (*R200 del*) KI allele in NPCs (Figure 5A). Within a subpopulation of cells overexpressing GFP-tagged PhiC31 and, therefore, lacking *Aifm1*, we could detect an obvious decreased content of CI*CIV-SCs compared with controls (Figures 5B and 5C). Second, we tested whether we could quantify the CI*CIV-SC content in a culture consisting of differentially treated cells. To do so, we transfected HeLa cells with scramble and siRNA against *AIFM1*, the latter inhibiting AIF expression (Figure 5D) and causing OXPHOS impairment and altered OCR (data not shown). We found that siAIF led to a decreased content of CI*CIV-SCs compared with scramble-treated cells (Figures 5E–5H). Having confirmed that, we cultured HeLa cells overexpressing mitochondria-targeted GFP and transfected them with scramble siRNA. Then, we mixed these cells with AIF-deficient HeLa cells (Figure 5I). Using GFP expression as a cellular marker, we could discriminate the two cell subpopulations and quantify the respective CI*CIV-SC content. As expected, scramble-transfected GFP-positive cells (control) had more PLA dots per cell compared with AIF (siAIF)-deficient HeLa (Figures 5J and 5K). This set of data already emphasizes the potential adaptability of our approach for image-based screens at the single-cell level. Third, we exposed HAP1 cells to mitochondrial toxins and quantified CI*CIV-SC content. Sequential as well as single addition of the ATP synthase inhibitor oligomycin, the protonophore FCCP, and CI/CIII inhibitors

(B) BN-PAGE and composite image of immunoblots using antibodies against NDUFB8 (CI) and MTCO1 (CIV, cropped bands for KI) using freshly frozen cerebella.
(C and D) Representative pictures of cerebellar Purkinje cells from 6-month-old control (C, WT) and Harlequin (D, Hq) mice stained with DAPI (nucleus), calbindin (Purkinje marker), TOM20 (mitochondria), and PLA (CI*CIV-SCs). Scale bar, 5 μm.
(E–I) Quantification of (E) area of the soma, (F) mitochondrial area, (G) mitochondria/soma ratio, (H) PLA-based dots normalized to the soma, (I) PLA-based dots normalized to the mitochondrial area. Data are represented as a violin plot with median (25th and 75th percentile), Student's *t*-test; n = 3; ***p < 0.001, **p < 0.01; ns, not significant.
(J) Linear correlation of PLA dots and mitochondrial area (WT, n = 3, 16 cells; Hq, n = 3, 22 cells). Linear regression, ns, not significant.
(K and L) Representative pictures of cerebellar Purkinje cells in control (K) (WT) and *Aifm1* (*R200 del*) KI (L) mice stained with DAPI (nucleus), calbindin (Purkinje marker), TOM20 (mitochondria), and PLA (CI*CIV-SCs). Scale bar: 5 μm.
(M–Q) Quantification of (M) area of the soma, (N) mitochondrial area, (O) mitochondria/soma ratio, (P) PLA-based dots normalized to the soma, (Q) PLA-based dots normalized to the mitochondrial area. Data are represented as a violin plot with median (25th and 75th percentile), n = 3, Student's t test, ****p < 0.0001, **p < 0.01, *p < 0.05, ns = not significant.
(R) linear correlation of PLA dots and mitochondrial area (WT, n = 3, 29 cells; KI, n = 3, 26 cells). Linear regression, ****p < 0.0001; ns, not significant.

CellPress
OPEN ACCESS

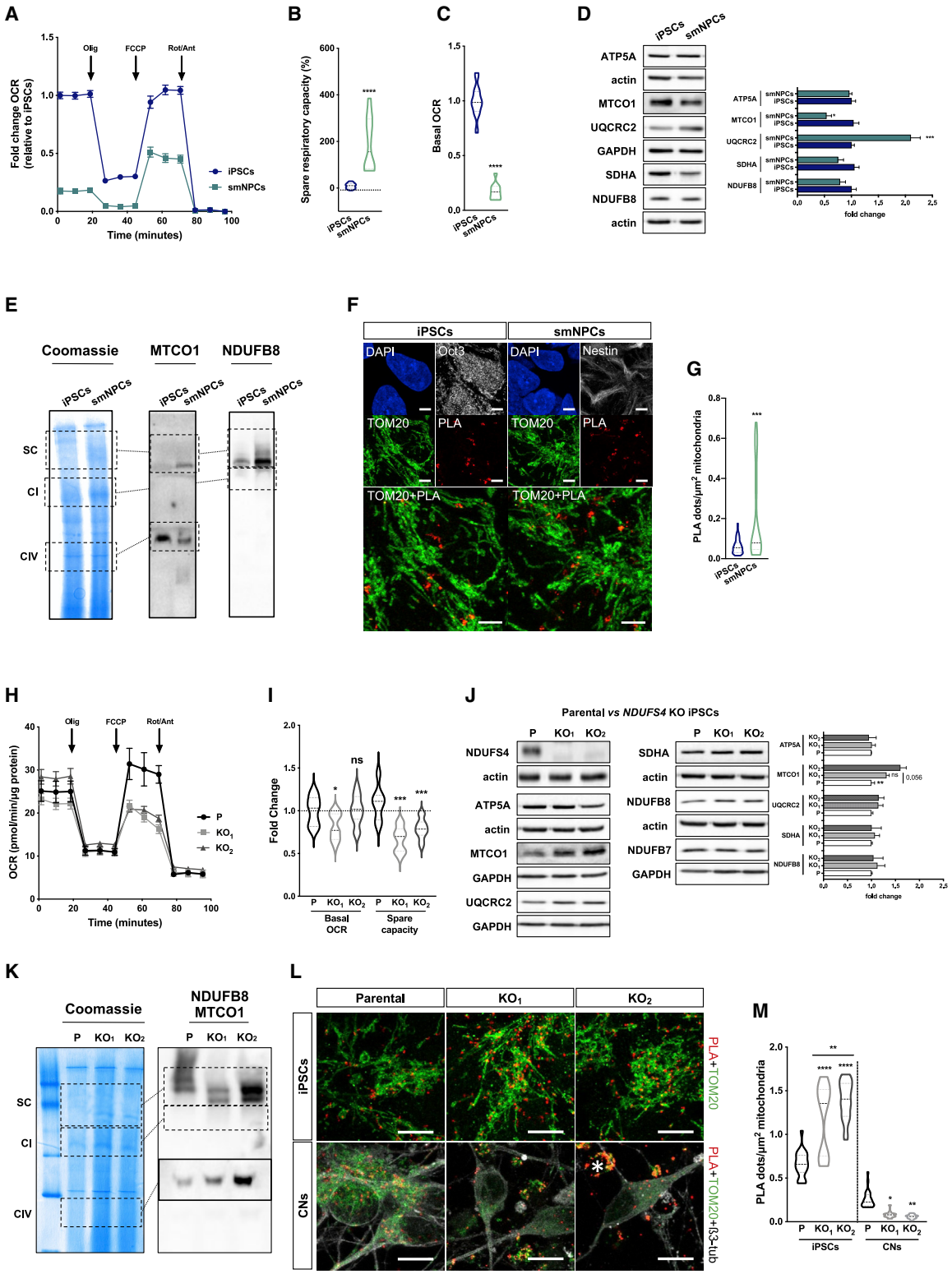

Figure 4. CI*CIV-SC remodeling occurs during iPSC differentiation

(A) OCR measurement of iPSCs and iPSC-derived smNPCs using a conventional Seahorse protocol (n = 3).

(B) Mitochondrial spare respiratory capacity in human iPSCs and smNPCs. Percentage is relative to their respective basal OCRs (Student's t test, ****$p < 0.0001$).

(C) Basal OCR in iPSCs and smNPCs (Student's t test, ****$p < 0.0001$).

(legend continued on next page)

(i.e., rotenone and antimycin A) resulted in mitochondrial respiratory adaptations corresponding to OCR profiles normally observed in tumorigenic cells (Figures S4A and S4B) (Connolly et al., 2018; Gioran et al., 2019). We found that 30 min exposure to mitochondrial respiratory inhibitors did not cause detectable expression changes of OXPHOS system components as revealed by immunostaining analysis (Figures S4C and S4D) and immunoblots (data not shown). Having profiled the response of HAP1 cells to these compounds, we assessed CI*CIV-SCs in control and drug-treated HAP1 cells. Compared with control, FCCP treatment affected neither mitochondrial area nor CI*-CIV-SC abundance (Figures 5L–5O), whereas both oligomycin- and rotenone and antimycin A-treated cells displayed a significant reduction of TOM20-labeled mitochondria associated with lower numbers of PLA-positive dots when normalized to mitochondrial content (Figures 5M and 5N). As a note, CI*CIV-SC contents reflected the trend observed in the Seahorse measurements (Figures S4A and S4B), with PLA numbers correlating with the mitochondrial respiration state upon drug treatments, possibly indicating an association between RSC abundance and OCR. These data further emphasize that CI*CIV-SC detection enables screens of small molecules or toxins that might influence mitochondrial respiration. Finally, we also performed PLA staining in hippocampal slices from the postmortem brain of a 71-year-old healthy donor (Figures S4E and S4F). We employed fluorescent as well as horseradish peroxidase-conjugated secondary antibodies, the latter staining as a standard technique in some clinical and diagnostic settings. Based on these first lines of evidence, it seems that our method enables both bright-field and fluorescent CI*CIV-SC visualization in fixed brain tissues from old healthy patients.

DISCUSSION

Mitochondrial OXPHOS generates large amounts of ATP and contributes to the maintenance of optimal NAD^+/NADH ratio in eukaryotic cells. At the crossroads of major metabolic pathways (Spinelli and Haigis, 2018), mitochondria host closely intertwined biochemical reactions that provide carbon units for fatty acid synthesis and gluconeogenesis as well as intermediates for the biogenesis of heme, nucleotide precursors, steroids, amino acids, and their derivatives. As a dynamic network of highly interconnected organelle units, mitochondria regulate cell death programs and intracellular calcium homeostasis (Berliocchi et al., 2005; Orrenius et al., 2003), thus integrating endogenous and exogenous cues into spatiotemporally defined signals that drive cellular adaptations and responses in different contexts. Because the maintenance and regulation of mitochondrial bioenergetics critically influence cellular homeostasis, a careful profiling of mitochondrial respiratory integrity serves as a sensitive indicator of the cellular metabolic state. Consistently, a comprehensive overview of mitochondrial paraments is particularly informative for understanding pathophysiological processes as well as for disease diagnosis and prognosis (Frazier et al., 2019; Connolly et al., 2018; Spinelli and Haigis, 2018; Koopman et al., 2016; Gorman et al., 2016).

We herein describe a method for the *in situ* detection of CI*-CIV-SCs in fixed cells as well as in tissues. Our established approach takes advantage of the physical distance between CI and CIV subunits when incorporated into superassembled structures. Given the well-characterized properties of PLA staining, we provide a consistent line of experimental evidence that supports a clear correlation between CI*CIV-SC numbers, composition, and organization of the OXPHOS system and functional changes in mitochondrial respiration. In a variety of biologically relevant settings, we report that single-cell quantification of CI*-CIV-SCs is technically feasible and represents a useful index for comparative analyses of mitochondrial ETC integrity and OXPHOS capacity. Our PLA-based protocol enables uniform signal patterns in the form of dot-like structures that, as fluorescent or bright-field stainings, are recognizable and quantifiable in either a manual or a semiautomated manner. In HeLa and near-haploid human HAP1 cells, NPCs, iPSCs, and iPSC-derived cortical neurons, tractable genetic lesions result in a decreased amount of CI*CIV-SCs that correlates with a general impairment of the OXPHOS system and consequent loss of cell fitness. Consistently, our data obtained in mouse-derived tissues further emphasize the sensitivity of our established assay in comparative investigations of mitochondrial defects associated with pathology. In the case of *Aifm1* (*R200 del*) KI mice, we were able to detect alterations of the OXPHOS system at single-cell

(D) Immunoblots using antibodies against OXPHOS system components in iPSCs and smNPCs. Densitometry is relative to iPSCs and reported as mean ± SEM (n = 3, Student's t test, ***p < 0.001, *p < 0.05).
(E) BN-PAGE and corresponding immunoblots using antibodies against MTCO1 and NDUFB8.
(F) Representative pictures of iPSCs and smNPCs stained with DAPI (nucleus, blue), TOM20 (mitochondria, green), and PLA (CI*CIV-SCs, red). Oct3 and nestin staining (both in gray) was used as markers of pluripotency and differentiation, respectively. Scale bar, 5 μm.
(G) Quantification of PLA dots normalized to mitochondrial area in iPSCs and smNPCs (n = 3; iPSCs = 20 cells; smNPCs = 17 cells; Student's t test, ***p < 0.001).
(H) OCR measurement of WT (P) and two independent clones of *NDUFS4* KO iPSCs (KO_1 and KO_2).
(I) Basal OCR and mitochondrial spare capacity of WT and *NDUFS4* KO iPSCs (fold change, relative to WT; two-way RM ANOVA, ***p < 0.001, *p < 0.05; ns, not significant).
(J) Immunoblot analysis of homogenates from parental and *NDUFS4* KO iPSCs using antibodies against ETC subunits (CI, NDUFS4, NDUFB7, and NDUFB8; CII, SDHA; CIII, UQCRC2; CIV, MTCO1; CV, ATP5A; actin and GAPDH as loading controls; n = 4; Student's t test, **p < 0.01).
(K) BN-PAGE and corresponding immunoblots using antibodies against MTCO1 and NDUFB8.
(L) Representative confocal images of parental and *NDUFS4* KO iPSCs and immature cortical neurons (CNs). Fluorescent staining of TOM20 (green) and β3-tubulin (gray) was used as mitochondrial and neuronal markers, respectively. PLA dots are in red. A dying cell is indicated with a white asterisk.
(M) Quantification of PLA dots normalized to the mitochondrial area in parental and *NDUFS4* KO iPSCs and immature cortical neurons (n = 3; WT iPSCs = 29 cells; *NDUFS4* KO_1 iPSCs = 21 cells; *NDUFS4* KO_2 iPSCs = 29 cells). Data are represented as a violin plot with median (25th and 75th percentile), one-way ANOVA, ****p < 0.0001, **p < 0.01, *p < 0.05.

CellPress
OPEN ACCESS

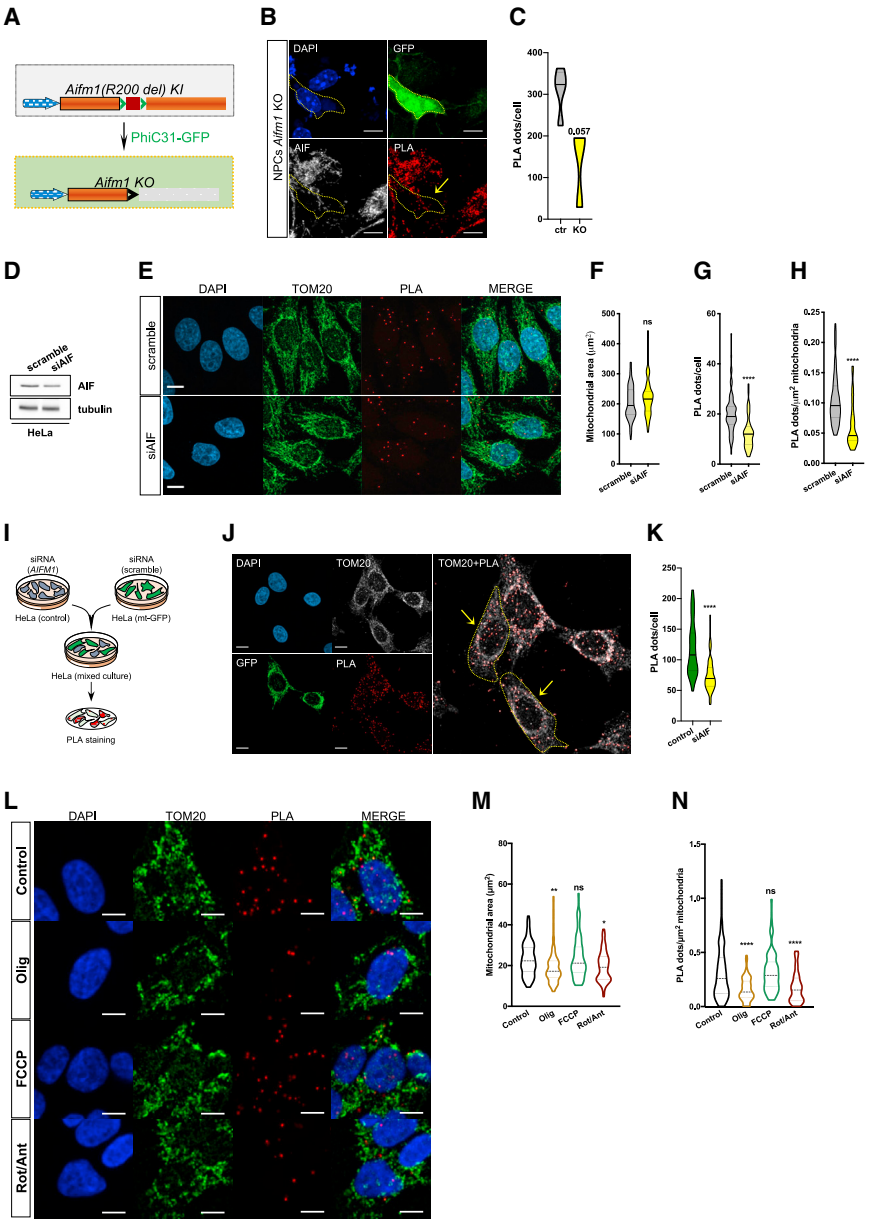

Figure 5. PLA-based imaging analysis of CI*CIV-SCs allows genetic screens in cultured cells

(A) Schematic representation of the *Aifm1*(*R200 del*) KI allele and its PhiC31-mediated recombination in NPCs. The two att sites (green arrowheads) flank exon 5 (red box) in the *Aifm1*(*R200 del*) KI allele. Upon transfection and overexpression of GFP-tagged PhiC31 recombinase, exon 5 is deleted and AIF expression is impaired.

(B) CI*CIV-SCs (PLA, red dots) in AIF KO NPCs generated from *Aifm1*(*R200 del*) KI mice. Loss of AIF was obtained by transfecting a plasmid encoding a GFP-tagged PhiC31 recombinase. A yellow dotted line delineates an AIF KO NPC (yellow arrow).

(C) Quantification of PLA dots/cell in control and AIF KO NPCs. Data are represented as a violin plot with median (25th and 75th percentile), n = 1, Student's t test, p = 0.057.

(D) Western blot analysis of HeLa cells transfected with scramble and siRNA against *AIFM1* (siAIF). Immunoblots were developed using antibodies against AIF and tubulin (as a loading control).

(E–H) Shown are (E) confocal images and quantification of (F) mitochondrial area (μm^2), (G) PLA dots per cell, and (H) PLA dots perμm^2 mitochondria of HeLa cells transfected with scramble and siRNA against *AIFM1* (n = 1, scramble = 70 cells, siAIF = 47 cells, Student's t test, ****p < 0.0001; ns, not significant).

(I) Schematic representation of the experiment. Control HeLa cells were transfected with siRNA against *AIFM1* for 24 h, while mitochondria-targeted GFP-overexpressing HeLa cells (mt-GFP) were transfected with scramble siRNA. Cells were then resuspended, mixed, and seeded on the same coverslip. After 24 h, the cells were fixed with paraformaldehyde and stained for TOM20 and CI*CIV-SCs.

(J and K) Shown are (J) representative confocal images and (K) quantification of PLA dots/cell in scramble-treated (control) and *AIFM1*-deficient (GFP negative, siAIF) cells, the latter highlighted by yellow dotted lines and arrows (n = 1, control = 44 cells, siAIF = 60 cells, Student's t test, ****p < 0.0001). Scale bar, 10 µm. DAPI was used to stain nuclei.

(L) Representative pictures of parental HAP1 cells treated with DMSO (Control), oligomycin (Olig), FCCP, and rotenone and antimycin A (Rot/Ant) and stained with DAPI (nucleus), TOM20 (mitochondria), and PLA (RSC). Scale bar, 5 µm.

(M and N) Quantification of (M) mitochondrial area and (N) PLA dots of CI*CIV-SCs normalized to the mitochondrial area (n = 3; control = 80 cells, oligomycin = 83 cells, FCCP = 63 cells, rotenone and antimycin A = 63 cells). Data are represented as a violin plot with median (25th and 75th percentile), one-way ANOVA with Bonferroni's post-hoc correction, ****p < 0.0001, **p < 0.01, *p < 0.05; ns, not significant.

resolution that were observed by using conventional biochemical methods (i.e., western blot analysis), but not with Seahorse respirometry. As an additional aspect supporting the robustness of our method, we were able to quantify neuron-specific ETC lesions in the cerebellum of Hq mutant mice, despite the extensive microgliosis that blunted other population-based analyses. Moreover, we effectively correlated the abundance of CI*CIV-SCs in iPSC and iPSC-derived NPCs. Our data imply that undifferentiated iPSCs have fewer CI*CIV-SCs, whereas partially committed iPSC-derived smNPCs exhibit an increased abundance of RSCs, possibly leading to enhanced mitochondrial spare respiratory capacity. As a consequence of *NDUFS4* loss of function, a condition often linked with human pathology, altered CI*CIV-SC content is associated with diminished survival of immature excitatory cortical neurons.

Apart from describing a validated method with major technical advantages, our study also addresses some unsettled biological questions. First, we report that our *in situ* PLA-based method

clearly reveals mitochondrial defects in tissues from "pre-symptomatic" (i.e., *Aifm1* [*R200 del*] KI with no obvious signs of cell death) as well as symptomatic (i.e., *Ndufs4* KO and Hq mutant) mice, whereas conventional Seahorse respirometry detected only marginal differences. By exploiting the sensitivity of our assay, we could discriminate and quantify cell-type-specific loss of mitochondrial ETC integrity in degenerating areas of Hq mutant brains. On the basis of the present and previous lines of evidence (Wischhof et al., 2018; Benit et al., 2008), we can conclude with confidence that these two mouse models of AIF deficiency bear equivalent mitochondrial defects, although they develop divergent neurodegenerative profiles. We speculate that reactive gliosis might be a trigger, rather than an associated feature, of neuronal demise in Hq mutant animals. Second, we describe that the abundance of RSCs, and in particular CI*CIV-SCs, depends on the metabolic and differentiation states of the cell, with increased RSCs in those cells that strongly rely on mitochondrial OXPHOS for energy production. In light of these considerations and our experimentally supported conclusions, we propose our PLA-based method as a valuable and complementary approach for single-cell comparative studies of mitochondrial fitness in complex organs, such as the brain.

Altogether, our findings using *in vitro* cell cultures and preclinical mouse models of mitochondrial diseases imply that single-cell assessment of CI*CIV-SCs is a quantifiable parameter of mitochondrial respiratory integrity. We envision that this method is suitable for a wide range of biomedical studies and might be adapted for diagnostic screenings of patient-derived materials.

Limitations of the study

Our method provides robustness and reproducibility when assessing CI*CIV-SCs at the single-cell level in fixed tissues. Moreover, it can be easily adapted for pharmacological or genetic screens that aim to investigate compounds or molecular factors influencing RSC biology and, indirectly, mitochondrial functionality. We recognize that our PLA protocol is time consuming, has only a few cost-benefit advantages, and might exhibit a reduced detection range when applied to systems that obtain ATP primarily from glycolysis, as in the case of cultured stem cells and tumorigenic cell lines. We are aware that our experiments were performed exclusively with one pair of highly validated antibodies and our PLA-based assessment of CI*CIV-SCs does not cover all possible superassembled species. Our method focuses primarily on RSC I_1+III_2+IV_1 and other eventual, uncharacterized superassembled structures containing NDUFB8 and MTCO1. Due to technical difficulties, we could not provide direct and mechanistic evidence that would conclusively elucidate the functional relevance of RSC abundance on mitochondrial oxygen consumption and ATP production as recently suggested (Calvo et al., 2020). Although feasible and marginally reported in our work (Figure S2C), we did not pursue the quantitative assessment of CI*CIV-SCs in neuronal projections, such as axons and dendrites. As a final consideration, we acknowledge a few limitations of our analysis as a proxy measurement of mitochondrial function/dysfunction. In this regard, our technique might not be able to discriminate between fully functional RSCs and NDUFB8- and MTCO1-containing assembly intermediates that accumulate because of stalled OXPHOS biogenesis. Because this aspect represents a potential confounding factor in discerning defects of mitochondrial bioenergetics, we set out to perform experiments by using *NDUFS4* KO iPSCs, knowing that NDUFS4 is part of the CI N-module and its incorporation occurs at a later stage and does not undermine the formation of RSC intermediates (Moreno-Lastres et al., 2012). In cells lacking NDUFS4 but still expressing normal levels of other OXPHOS subunits (e.g., ATP5A, MTCO1, UQCRC2, SDHA, NDUFB8, and NDUFB7), we report that the increased number of CI*CIV-SCs correlates with the enhanced formation of RSC assembly intermediates. Although these data might sound surprising, they are consistent with previous evidence elucidating the incorporation of ETC subunits at different stages (Moreno-Lastres et al., 2012; Protasoni et al., 2020; Lobo-Jarne et al., 2020). At least in undifferentiated iPSCs, Seahorse measurements could detect defects in mitochondrial bioenergetics, whereas our study of CI*CIV-SCs would suggest a different scenario. Thus, we call for attention when interpreting PLA-based CI*CIV-SC quantifications that are not corroborated by complementary methods.

STAR★METHODS

Detailed methods are provided in the online version of this paper and include the following:

- KEY RESOURCES TABLE
- RESOURCE AVAILABILITY
  - Lead contact
  - Materials availability
  - Data and code availability
- EXPERIMENTAL MODEL AND SUBJECT DETAILS
  - Cell lines and culture conditions
  - Mouse models
  - Postmortem human tissues
- METHOD DETAILS
  - Imaging analysis and PLA quantification
  - Native polyacrylamide gel electrophoresis, SDS gel electrophoresis and western blot analysis
  - Oxygen consumption rate measurements
  - Proximity ligation assay (PLA) fluorescence
  - Proximity ligation assay (PLA) brightfield
- QUANTIFICATION AND STATISTICAL ANALYSIS

SUPPLEMENTAL INFORMATION

Supplemental information can be found online at https://doi.org/10.1016/j.crmeth.2021.100002.

ACKNOWLEDGMENTS

We wish to thank our DZNE colleagues at LMF, Ms. Christiane Bartling-Kirsch for her assistance, Professor Donato Di Monte and Professor Werner Koopman for their critical comments, and the Netherland Brain Bank (NBB) for the human postmortem tissues kindly provided for this work. This research was supported by the DZNE institutional budget, the CoEN (Carbon-Model, 3018) initiative, and the Helmholtz cross-program topic "Aging and Metabolic

Programming (AMPro)." F.B. and A.M.-C. received funding from the European Union's Horizon 2020 research and innovation program under Marie Skłodowska-Curie grant agreement 676144 (Synaptic Dysfunction in Alzheimer Disease, SyDAD). L.W., P.N., and D.B. are members of the DFG Cluster of Excellence ImmunoSensation funded by the Deutsche Forschungsgemeinschaft (DFG, German Research Foundation) under Germany's Excellence Strategy – EXC2151 – 390873048. J.J., J.H.M.P., and D.B. are members of the Mitochondrial Dysfunction in Parkinson's Consortium (PD-MitoQUANT). PD-MitoQUANT has received funding from the Innovative Medicines Initiative 2 Joint Undertaking under grant agreement 821522. This joint undertaking receives support from the European Union's Horizon 2020 research and innovation program and EFPIA.

AUTHOR CONTRIBUTIONS

Conceptualization, F.B., L.W., and D.B.; methodology, F.B., M.G., A.M.C., L.W., and M.P.; validation, formal analysis, investigation, resources, and data curation, F.B., L.W., E.S., M.G., J.J., A.M.C., A.P., M.S., and M.P.; writing – original draft, F.B. and D.B.; writing – review & editing, F.B. and D.B.; visualization, F.B., L.W., and D.B.; supervision, F.B. and D.B.; project administration, D.B.; funding acquisition, M.P., J.H.M.P., P.N., and D.B.

DECLARATION OF INTERESTS

The authors declare no competing interests.

Received: September 28, 2020
Revised: February 3, 2021
Accepted: March 3, 2021
Published: April 2, 2021

REFERENCES

Acin-Perez, R., Fernandez-Silva, P., Peleato, M.L., Perez-Martos, A., and Enriquez, J.A. (2008). Respiratory active mitochondrial supercomplexes. Mol. Cell *32*, 529–539.

Area-Gomez, E., and Schon, E.A. (2014). Mitochondrial genetics and disease. J. Child Neurol. *29*, 1208–1215.

Bano, D., and Prehn, J.H.M. (2018). Apoptosis-inducing factor (AIF) in physiology and disease: the tale of a repented natural born killer. EBioMedicine *30*, 29–37.

Benit, P., Goncalves, S., Dassa, E.P., Briere, J.J., and Rustin, P. (2008). The variability of the harlequin mouse phenotype resembles that of human mitochondrial-complex I-deficiency syndromes. PLoS One *3*, e3208.

Berliocchi, L., Bano, D., and Nicotera, P. (2005). Ca2+ signals and death programmes in neurons. Philos. Trans. R. Soc. Lond. B Biol. Sci. *360*, 2255–2258.

Berndtsson, J., Aufschnaiter, A., Rathore, S., Marin-Buera, L., Dawitz, H., Diessl, J., Kohler, V., Barrientos, A., Buttner, S., Fontanesi, F., and Ott, M. (2020). Respiratory supercomplexes enhance electron transport by decreasing cytochrome c diffusion distance. EMBO Rep. *21*, e51015.

Bianchi, C., Genova, M.L., Parenti Castelli, G., and Lenaz, G. (2004). The mitochondrial respiratory chain is partially organized in a supercomplex assembly: kinetic evidence using flux control analysis. J. Biol. Chem. *279*, 36562–36569.

Blaza, J.N., Serreli, R., Jones, A.J., Mohammed, K., and Hirst, J. (2014). Kinetic evidence against partitioning of the ubiquinone pool and the catalytic relevance of respiratory-chain supercomplexes. Proc. Natl. Acad. Sci. U S A *111*, 15735–15740.

Calvaruso, M.A., Willems, P., Van Den Brand, M., Valsecchi, F., Kruse, S., Palmiter, R., Smeitink, J., and Nijtmans, L. (2012). Mitochondrial complex III stabilizes complex I in the absence of NDUFS4 to provide partial activity. Hum. Mol. Genet. *21*, 115–120.

Calvo, E., Cogliati, S., Hernansanz-Agustin, P., Loureiro-Lopez, M., Guaras, A., Casuso, R.A., Garcia-Marques, F., Acin-Perez, R., Marti-Mateos, Y., Silla-Castro, J.C., et al. (2020). Functional role of respiratory supercomplexes in mice: SCAF1 relevance and segmentation of the Qpool. Sci. Adv. *6*, eaba7509.

Calvo, S.E., Clauser, K.R., and Mootha, V.K. (2016). MitoCarta2.0: an updated inventory of mammalian mitochondrial proteins. Nucleic Acids Res. *44*, D1251–D1257.

Cogliati, S., Calvo, E., Loureiro, M., Guaras, A.M., Nieto-Arellano, R., Garcia-Poyatos, C., Ezkurdia, I., Mercader, N., Vazquez, J., and Enriquez, J.A. (2016). Mechanism of super-assembly of respiratory complexes III and IV. Nature *539*, 579–582.

Connolly, N.M.C., Theurey, P., Adam-Vizi, V., Bazan, N.G., Bernardi, P., Bolanos, J.P., Culmsee, C., Dawson, V.L., Deshmukh, M., Duchen, M.R., et al. (2018). Guidelines on experimental methods to assess mitochondrial dysfunction in cellular models of neurodegenerative diseases. Cell Death Differ. *25*, 542–572.

Fedor, J.G., and Hirst, J. (2018). Mitochondrial supercomplexes do not enhance catalysis by quinone channeling. Cell Metab. *28*, 525–531 e4.

Frazier, A.E., Thorburn, D.R., and Compton, A.G. (2019). Mitochondrial energy generation disorders: genes, mechanisms, and clues to pathology. J. Biol. Chem. *294*, 5386–5395.

Frazier, A.E., Vincent, A.E., Turnbull, D.M., Thorburn, D.R., and Taylor, R.W. (2020). Assessment of mitochondrial respiratory chain enzymes in cells and tissues. Methods Cell Biol. *155*, 121–156.

Fredriksson, S., Gullberg, M., Jarvius, J., Olsson, C., Pietras, K., Gustafsdottir, S.M., Ostman, A., and Landegren, U. (2002). Protein detection using proximity-dependent DNA ligation assays. Nat. Biotechnol. *20*, 473–477.

Fried, N.T., Moffat, C., Seifert, E.L., and Oshinsky, M.L. (2014). Functional mitochondrial analysis in acute brain sections from adult rats reveals mitochondrial dysfunction in a rat model of migraine. Am. J. Physiol. Cell Physiol. *307*, C1017–C1030.

Garcia-Poyatos, C., Cogliati, S., Calvo, E., Hernansanz-Agustin, P., Lagarrigue, S., Magni, R., Botos, M., Langa, X., Amati, F., Vazquez, J., et al. (2020). Scaf1 promotes respiratory supercomplexes and metabolic efficiency in zebrafish. EMBO Rep. *21*, e50287.

Gioran, A., Piazzesi, A., Bertan, F., Schroer, J., Wischhof, L., Nicotera, P., and Bano, D. (2019). Multi-omics identify xanthine as a pro-survival metabolite for nematodes with mitochondrial dysfunction. EMBO J. *38*, e99558.

Gorman, G.S., Chinnery, P.F., Dimauro, S., Hirano, M., Koga, Y., Mcfarland, R., Suomalainen, A., Thorburn, D.R., Zeviani, M., and Turnbull, D.M. (2016). Mitochondrial diseases. Nat. Rev. Dis. Primers *2*, 16080.

Greggio, C., Jha, P., Kulkarni, S.S., Lagarrigue, S., Broskey, N.T., Boutant, M., Wang, X., Conde Alonso, S., Ofori, E., Auwerx, J., et al. (2017). Enhanced respiratory chain supercomplex formation in response to exercise in human skeletal muscle. Cell Metab. *25*, 301–311.

Gu, J., Wu, M., Guo, R., Yan, K., Lei, J., Gao, N., and Yang, M. (2016). The architecture of the mammalian respirasome. Nature *537*, 639–643.

Guo, R., Zong, S., Wu, M., Gu, J., and Yang, M. (2017). Architecture of human mitochondrial respiratory megacomplex I2III2IV2. Cell *170*, 1247–1257.e12.

Hackenbrock, C.R., Chazotte, B., and Gupte, S.S. (1986). The random collision model and a critical assessment of diffusion and collision in mitochondrial electron transport. J. Bioenerg. Biomembr. *18*, 331–368.

Katajisto, P., Dohla, J., Chaffer, C.L., Pentinmikko, N., Marjanovic, N., Iqbal, S., Zoncu, R., Chen, W., Weinberg, R.A., and Sabatini, D.M. (2015). Stem cells. Asymmetric apportioning of aged mitochondria between daughter cells is required for stemness. Science *348*, 340–343.

Klein, J.A., Longo-Guess, C.M., Rossmann, M.P., Seburn, K.L., Hurd, R.E., Frankel, W.N., Bronson, R.T., and Ackerman, S.L. (2002). The harlequin mouse mutation downregulates apoptosis-inducing factor. Nature *419*, 367–374.

Koopman, W.J., Beyrath, J., Fung, C.W., Koene, S., Rodenburg, R.J., Willems, P.H., and Smeitink, J.A. (2016). Mitochondrial disorders in children: toward development of small-molecule treatment strategies. EMBO Mol. Med. *8*, 311–327.

Kruse, S.E., Watt, W.C., Marcinek, D.J., Kapur, R.P., Schenkman, K.A., and Palmiter, R.D. (2008). Mice with mitochondrial complex I deficiency develop a fatal encephalomyopathy. Cell Metab. *7*, 312–320.

Lake, N.J., Compton, A.G., Rahman, S., and Thorburn, D.R. (2016). Leigh syndrome: one disorder, more than 75 monogenic causes. Ann. Neurol. *79*, 190–203.

Lapuente-Brun, E., Moreno-Loshuertos, R., Acin-Perez, R., Latorre-Pellicer, A., Colas, C., Balsa, E., Perales-Clemente, E., Quiros, P.M., Calvo, E., Rodriguez-Hernandez, M.A., et al. (2013). Supercomplex assembly determines electron flux in the mitochondrial electron transport chain. Science *340*, 1567–1570.

Letts, J.A., Fiedorczuk, K., Degliesposti, G., Skehel, M., and Sazanov, L.A. (2019). Structures of respiratory supercomplex I+III2 reveal functional and conformational crosstalk. Mol. Cell *75*, 1131–1146.e6.

Letts, J.A., Fiedorczuk, K., and Sazanov, L.A. (2016). The architecture of respiratory supercomplexes. Nature *537*, 644–648.

Lisowski, P., Kannan, P., Mlody, B., and Prigione, A. (2018). Mitochondria and the dynamic control of stem cell homeostasis. EMBO Rep. *19*, e45432.

Lobo-Jarne, T., Perez-Perez, R., Fontanesi, F., Timon-Gomez, A., Wittig, I., Penas, A., Serrano-Lorenzo, P., Garcia-Consuegra, I., Arenas, J., Martin, M.A., et al. (2020). Multiple pathways coordinate assembly of human mitochondrial complex IV and stabilization of respiratory supercomplexes. EMBO J. *39*, e103912.

Lopez-Fabuel, I., Le Douce, J., Logan, A., James, A.M., Bonvento, G., Murphy, M.P., Almeida, A., and Bolanos, J.P. (2016). Complex I assembly into supercomplexes determines differential mitochondrial ROS production in neurons and astrocytes. Proc. Natl. Acad. Sci. U S A *113*, 13063–13068.

Maranzana, E., Barbero, G., Falasca, A.I., Lenaz, G., and Genova, M.L. (2013). Mitochondrial respiratory supercomplex association limits production of reactive oxygen species from complex I. Antioxid. Redox Signal. *19*, 1469–1480.

Meyer, K., Buettner, S., Ghezzi, D., Zeviani, M., Bano, D., and Nicotera, P. (2015). Loss of apoptosis-inducing factor critically affects MIA40 function. Cell Death Dis. *6*, e1814.

Mimaki, M., Wang, X., Mckenzie, M., Thorburn, D.R., and Ryan, M.T. (2012). Understanding mitochondrial complex I assembly in health and disease. Biochim. Biophys. Acta *1817*, 851–862.

Moreno-Lastres, D., Fontanesi, F., Garcia-Consuegra, I., Martin, M.A., Arenas, J., Barrientos, A., and Ugalde, C. (2012). Mitochondrial complex I plays an essential role in human respirasome assembly. Cell Metab. *15*, 324–335.

Mourier, A., Matic, S., Ruzzenente, B., Larsson, N.G., and Milenkovic, D. (2014). The respiratory chain supercomplex organization is independent of COX7a2l isoforms. Cell Metab. *20*, 1069–1075.

Orrenius, S., Zhivotovsky, B., and Nicotera, P. (2003). Regulation of cell death: the calcium-apoptosis link. Nat. Rev. Mol. Cell Biol. *4*, 552–565.

Pagliarini, D.J., Calvo, S.E., Chang, B., Sheth, S.A., Vafai, S.B., Ong, S.E., Walford, G.A., Sugiana, C., Boneh, A., Chen, W.K., et al. (2008). A mitochondrial protein compendium elucidates complex I disease biology. Cell *134*, 112–123.

Peitz, M., Krutenko, T., and Brüstle, O. (2020). Protocol for the standardized generation of forward programmed cryopreservable excitatory and inhibitory forebrain neurons. STAR Protoc. *1*, 1–14.

Protasoni, M., Perez-Perez, R., Lobo-Jarne, T., Harbour, M.E., Ding, S., Penas, A., Diaz, F., Moraes, C.T., Fearnley, I.M., Zeviani, M., et al. (2020). Respiratory supercomplexes act as a platform for complex III-mediated maturation of human mitochondrial complexes I and IV. EMBO J. *39*, e102817.

Quintana, A., Kruse, S.E., Kapur, R.P., Sanz, E., and Palmiter, R.D. (2010). Complex I deficiency due to loss of Ndufs4 in the brain results in progressive encephalopathy resembling Leigh syndrome. Proc. Natl. Acad. Sci. U S A *107*, 10996–11001.

Rhee, H.J., Shaib, A.H., Rehbach, K., Lee, C., Seif, P., Thomas, C., Gideons, E., Guenther, A., Krutenko, T., Hebisch, M., et al. (2019). An autaptic culture system for standardized analyses of iPSC-derived human neurons. Cell Rep. *27*, 2212–2228 e7.

Schagger, H., De Coo, R., Bauer, M.F., Hofmann, S., Godinot, C., and Brandt, U. (2004). Significance of respirasomes for the assembly/stability of human respiratory chain complex I. J. Biol. Chem. *279*, 36349–36353.

Schagger, H., and Pfeiffer, K. (2000). Supercomplexes in the respiratory chains of yeast and mammalian mitochondria. EMBO J. *19*, 1777–1783.

Schagger, H., and Pfeiffer, K. (2001). The ratio of oxidative phosphorylation complexes I-V in bovine heart mitochondria and the composition of respiratory chain supercomplexes. J. Biol. Chem. *276*, 37861–37867.

Spinelli, J.B., and Haigis, M.C. (2018). The multifaceted contributions of mitochondria to cellular metabolism. Nat. Cell Biol. *20*, 745–754.

Sun, D., Li, B., Qiu, R., Fang, H., and Lyu, J. (2016). Cell type-specific modulation of respiratory chain supercomplex organization. Int. J. Mol. Sci. *17*, 926.

Troulinaki, K., Buttner, S., Marsal Cots, A., Maida, S., Meyer, K., Bertan, F., Gioran, A., Piazzesi, A., Fornarelli, A., Nicotera, P., and Bano, D. (2018). WAH-1/AIF regulates mitochondrial oxidative phosphorylation in the nematode Caenorhabditis elegans. Cell Death Discov. *4*, 2.

Wallace, D.C. (2018). Mitochondrial genetic medicine. Nat. Genet. *50*, 1642–1649.

Wischhof, L., Gioran, A., Sonntag-Bensch, D., Piazzesi, A., Stork, M., Nicotera, P., and Bano, D. (2018). A disease-associated Aifm1 variant induces severe myopathy in knockin mice. Mol. Metab. *13*, 10–23.

Wu, M., Gu, J., Guo, R., Huang, Y., and Yang, M. (2016). Structure of mammalian respiratory supercomplex I1III2IV1. Cell *167*, 1598–1609 e10.

STAR★METHODS

KEY RESOURCES TABLE

REAGENT or RESOURCE	SOURCE	IDENTIFIER
Antibodies		
Rabbit anti-TOM20 polyclonal antibody	Santa Cruz Biotechnology	Cat# sc-11415; RRID:AB_2207533
Rabbit anti-NDUFB8 polyclonal antibody	Proteintech	Cat# 14794-1-AP; RRID:AB_2150970
Mouse anti-MTCO1 monoclonal antibody	Abcam	Cat# ab14705; RRID:AB_2084810
Mouse anti-calbindin D-28K monoclonal antibody	Swant	Cat# 300; RRID:AB_10000347
Mouse anti-VDAC1/porin monoclonal antibody	Abcam	Cat# ab14734; RRID:AB_443084
Goat anti-rabbit IgG (H+L) highly cross-adsorbed secondary antibody, Alexa Fluor 633	Invitrogen, Thermo Fisher	Cat# A-21071; RRID:AB_2535732
Goat anti-mouse IgG (H+L) highly cross-adsorbed secondary antibody, Alexa Fluor 633	Invitrogen, Thermo Fisher	Cat# A-21052; RRID:AB_2535719
Goat anti-rabbit IgG (H+L) cross-adsorbed secondary antibody, Alexa Fluor 488	Invitrogen, Thermo Fisher	Cat# A-11008; RRID:AB_143165
Goat anti-mouse IgG, IgM (H+L) secondary antibody, Alexa Fluor 488	Invitrogen, Thermo Fisher	Cat# A-10680; RRID:AB_2534062
Goat anti-mouse IgG (H+L) highly cross-adsorbed secondary antibody, Alexa Fluor 568	Invitrogen, Thermo Fisher	Cat# A-11031; RRID:AB_144696
Goat anti-rabbit IgG (H+L) cross-adsorbed secondary antibody, Alexa Fluor 568	Invitrogen, Thermo Fisher	Cat# A-11011; RRID:AB_14315
Mouse anti-beta-actin monoclonal antibody, Unconjugated, Clone AC-74	SIGMA	Cat# A5316; RRID:AB_476743
Mouse anti-AIF (E-1) monoclonal antibody	Santa Cruz Biotechnology	Cat# sc-13116; RRID:AB_626654
Total OXPHOS rodent WB antibody cocktail	Abcam	Cat# ab110413; RRID:AB_2629281
Rabbit anti-COX IV polyclonal antibody	Cell Signaling Technology	Cat# 4844; RRID:AB_2085427
Mouse anti-NeuN monoclonal antibody	Millipore	Cat# MAB377; RRID:AB_2298772
Rabbit anti-GAPDH polyclonal Antibody (FL-335)	Santa Cruz Biotechnology	Cat# sc-25778; RRID:AB_10167668
Mouse anti-βIII tubulin mAb antibody	Promega	Cat# G7121; RRID:AB_430874
Mouse Anti-NDUFA9 monoclonal antibody, unconjugated, clone 20C11	Abcam	Cat# ab14713; RRID:AB_301431
Mouse anti-UQCRC2 Monoclonal antibody [13G12AF12BB11]	Abcam	Cat# ab14745; RRID:AB_2213640
Rabbit Anti-UQCRC2 Monoclonal antibody [EPR13051]	Abcam	Cat# ab203832; RRID:AB_2797139
Mouse anti-ATP5A monoclonal [15H4C4] antibody	Abcam	Cat# ab14748; RRID:AB_301447
Mouse anti-SDHA monoclonal antibody	Thermo Fisher	Cat# 459200; RRID:AB_2532231
Rabbit NDUFB7 polyclonal antibody	Proteintech	Cat# 14912-1-AP; RRID:AB_2235903
Rat anti-OCT3/4 monoclonal antibody (EM92)	Thermo Fisher	Cat# 14-5841-82; RRID:AB_914301
Mouse anti-nestin monoclonal (clone#196908) antibody	R&D Systems	Cat# MAB1259; RRID:AB_2251304
Mouse anti-NDUFS4 monoclonal [2C7CD4AG3] antibody	Abcam	Cat# ab87399; RRID:AB_10865698
Duolink In Situ PLA Probe Anti-Mouse Minus	SIGMA	Cat# DUO9004
Duolink In Situ PLA Probe Anti-Mouse Plus	SIGMA	Cat# DUO92001
Duolink In Situ PLA Probe Anti-Rabbit Minus	SIGMA	Cat# DUO92005

(*Continued on next page*)

Continued

REAGENT or RESOURCE	SOURCE	IDENTIFIER
Duolink In Situ PLA Probe Anti-Rabbit Plus	SIGMA	Cat# DUO92002
Duolink In Situ Detection Brighfield	SIGMA	Cat# DUO92012
Duolink In Situ Detection Reagents Red	SIGMA	Cat# DUO92008
Biological samples		
Healthy adult human hippocampal brain samples	The Netherlands Brain Bank (NBB) https://www.brainbank.nl/	nbb 1995-097, S95/281, female
Chemicals, peptides, and recombinant proteins		
Accutase	Gibco	Cat# A11105-01
Antimycin A	SIGMA	Cat# A8674
Cytosine-1-beta-D-arabinofuranoside (AraC)	Merck	Cat# C1768
B-27 supplement (50x)	Gibco	Cat# 12587-010
Carbonyl cyanide-p-trifluoromethoxyphenylhydrazone (FCCP)	SIGMA	C2920
CHIR99021	Milteny Biotech	Cat# 130-106-539
DMEM/F12	Gibco	Cat# 11320-074
Doxycycline	SIGMA	Cat# D9891-1G
GlutaMAX	Gibco	Cat# 35050-38
Laminin	SIGMA	Cat# L2020
Lipofectamine 3000	Thermo Fisher	Cat# L3000-008
N2 Supplement (100x)	GE Healthcare	Cat# T11292005
Neurobasal	Gibco	Cat# 21103-049
Oligomycin	SIGMA	Cat# 75351
Purmorphamine	Milteny Biotech	Cat# 13-104-465
ROCK inhibitor	Cellagen Technology LLC	Cat# C9127-2
Rotenone	SIGMA	Cat# R8875
StemMACS iPS-Brew 50x supplement	Milteny Biotech	Cat# 130-107-86
StemMACS iPS-Brew	Milteny Biotech	Cat# 130-107-87
Vitronectin	Thermo Fisher	Cat# A14700
Critical commercial assays		
Duolink In Situ Detection Reagents Red	SIGMA	Cat# DUO92008
Duolink In Situ Detection Reagents Brightfield	SIGMA	Cat# DUO92012
Seahorse XF Cell Mito Stress Test Kit	Agilent	Cat# 103015-100
Amaxa® nucleofection kit V	Lonza	Cat# VVSA-1003
NativePAGE™ 3 to 12%, Bis-Tris, 1.0 mm, Mini Protein Gel	Invitrogen, Thermo Fisher	Cat# BN1001BOX
NOVEX Colloidal blue staining kit	Invitrogen, Thermo Fisher	Cat# LC6025
Experimental models: cell lines		
Human HAP1 parental	Horizon Discovery	C631
Human HAP1 NDUFS2	Horizon Discovery	(Gioran et al., 2019)
Human HAP1 NDUFS4	Horizon Discovery	(Gioran et al., 2019)
Human HeLa cells	ATCC	ATCC CCL-2
Human iPS cell line C-14m-s11-NGN2	Dr. Michael Peitz, University of Bonn	(Rhee et al., 2019)
Human iPS cell line, *NDUFS4* KO	This manuscript	
Experimental models: organisms/strains		
Mouse: C57BL/J6	The Jackson Laboratory (JAX)	JAX: 000664
Mouse: B6CBACa $A^{w\text{-}J}$/*A-Aifm1*^{Hq}/J	The Jackson Laboratory (JAX)	JAX: 000501

(*Continued on next page*)

Continued

REAGENT or RESOURCE	SOURCE	IDENTIFIER
Mouse: B6.129S4-*Ndufs4*$^{tm1.1Rpa}$/J	The Jackson Laboratory (JAX)	JAX: 027058
Mouse: *Aifm1 (R200 del)* knockin mice	Dr. Daniele Bano, DZNE	(Wischhof et al., 2018)
Oligonucleotides		
CRISPR-Cas9 target sequence: tracrRNA:crRNA: GGTCGTTGAGGACTTCCACA	Integrated DNA Technologies (IDT)	Cat# 1072533
siRNA AIFM1	Ambion, Thermo Fisher	ID 117234
siRNA negative control sequence	Ambion, Thermo Fisher	AM4611
siRNA siNDUFS3	Ambion, Thermo Fisher	ID s224103
Recombinant DNA		
Plasmid: PhiC31-GFP	System Biosciences (SBI)	FC200PA-1
Software and algorithms		
Image J	U.S. National Institutes of Health, Bethesda, Maryland, USA	https://imagej.nih.gov/ij/
GraphPad Prism 8	GraphPad Software Inc., Boston, USA	https://www.graphpad.com/scientific-software/prism/
Imaris	Bitplane	https://imaris.oxinst.com/
ICE Synthego	Synthego Corporation	https://ice.synthego.com/#/

RESOURCE AVAILABILITY

Lead contact

Further information and requests for resources and reagents should be directed and will be fulfilled by the Lead Contact, Dr. Daniele Bano (daniele.bano@dzne.de).

Materials availability

All newly generated items used in this study are available upon request and following standard Material Transfer Agreement (MTA), due to institutional recommendations.

Data and code availability

This study did not generate computer algorithm or code.

EXPERIMENTAL MODEL AND SUBJECT DETAILS

Cell lines and culture conditions

Near-haploid HAP1 cells (Horizon Genomic's GmbH, Vienna, Austria) were grown at 37°C in Iscove's modified Dulbecco medium (IMDM) supplemented with 10% fetal bovine serum and 1% penicillin/streptomycin (100 U/mL penicillin; 100 μg/mL streptomycin). Parental and mitochondrial mutant HAP1 cells were maintained and used as previously described (Gioran et al., 2019). Drug treatments with oligomycin, FCCP, rotenone/antimycin A in HAP1 cells were carried out for 30 min following the concentrations used for Seahorse experiments (Connolly et al., 2018). iPSCs were cultured at 37°C under feeder-free conditions in StemMACs iPS-Brew (Miltenyi Biotec) on vitronectin-coated 6-well plates with daily medium changes. For OCR measurements (see below), iPSCs were split with EDTA and $5x10^4$ cells per well were seeded on Seahorse XF24 cell culture microplates (Agilent) 24 h before the experiment. For PLA-experiments, $1x10^5$ cells per well were seeded on vitronectin-coated coverslips in 12-well plates, and fixed with 4% PFA on the next day. iPSCs-derived small molecule neural precursor cells (smNPCs) were cultured on Matrigel-coated 6-well plates and kept in N2B27 medium consisting of DMEM-F12 (Invitrogen)/Neurobasal (Invitrogen) with N2 and B27 (without vitamin A) supplement, 1% glutamine, 0.5 μM Purmorphamine (Miltenyi Biotec), 3 μM CHIR 99021 (Miltenyi Biotec) and 150 μM LAAP (Merck). Medium was replaced every other day. For OCR measurements, smNPCs were split with accutase and $2x10^5$ cells per well were seeded on Seahorse cell culture microplates (Agilent) one day before the experiment. For PLA experiments, $3x10^5$ cells per well were seeded on Matrigel-coated coverslips in 12-well plates and fixed with 4% PFA 48 to 72 h after seeding. smNPCs were spontaneously differentiated by withdrawal of supplements from the N2B27 medium. After three weeks, cultures were mitotically inactivated by treatment

with 5 μM AraC, resulting in a predominant neuronal population with less than 1% glia cells (data not shown). Cells were differentiated for a total of 4 to 5 weeks with medium changes every other day. For PLA experiments, 1x10^5 smNPCs per well were seeded on Matrigel-coated coverslips in 12-well plates, switched to differentiation medium the next day, and fixed with 4 % PFA after 4 to 5 weeks of differentiation.

HeLa cells were grown at 37°C in DMEM supplemented with 10% fetal bovine serum and 1% penicillin/streptomycin (100 U/ml penicillin; 100 μg/ml streptomycin). For lipid-mediated siRNA transfection, cells were trypsinized and seeded onto glass coverslips in 24-well plates (3 x 10^4 cells/well) together with transfection complexes (Lipofectamine 3000 and siRNAs at a final concentration of 100 nM) diluted in Opti-MEM. After 48 h, cells were fixed in 4% PFA and used for PLA experiments. The following siRNAs were used: negative control AM4611, siAIFM1 ID 117234, siNDUFS3 ID s224103 (Ambion, Thermo Fisher).

To generate *NDUFS4* KO iPSCs, we used human iPS cell line C-14m-s11-NGN2, which carries a doxycycline-inducible NGN2 transgene that enables rapid forward programming into excitatory neurons (Rhee et al., 2019). Cells were nucleofected with a CRISPR-Cas9 ribonucleoprotein (RNP) complex containing Alt-R HiFi Cas9 Nuclease (IDT) and a tracrRNA:crRNA duplex (crRNA sequence: GGTCGTTGAGGACTTCCACA) using program CM150 of the Amaxa 4D Nucleofector (Lonza). Briefly, the transfection solution (16.4 μl P3 solution, 3.6 μl supplement 1, 0.5 μl electroporation enhancer and 2.5 μl RNP mix) consisted of equal volumes of Cas9 protein (from 61 μM stock) and an annealed tracrRNA:crRNA duplex solution (all reagents were purchased from IDT, USA). Nucleofection was performed with 20 μl of the transfection solution. From the resulting genome-edited polyclonal cell line, single cell-derived sub-clones were isolated. Frameshift-inducing mutations were identified by Sanger sequencing. Single clones were selected if they showed a Knockout Score of at least 99% according to the ICE CRISPR Analysis Tool (www.synthego.com). Sequence-validated clones were further expanded and quality-controlled by virtual karyotyping using SNP arrays and regular mycoplasma testing. Candidate C-14m-s11-NGN2 clones were then differentiated into excitatory neurons following a previously published protocol (Peitz et al., 2020).

Mouse models

Aifm1 (R200 del) knockin mice were generated as previously described (Wischhof et al., 2018). B6.129S4-*Ndufs4*$^{tm1.1Rpa}$/J (Jax Stock No 027058 and B6CBACa *A*$^{w-J}$/*A-Aifm1*^{Hq}/J (Jax Stock No 000501) were obtained from The Jackson Laboratory (Bar harbor, Maine, USA). All mice were housed under a 12/12 h light/dark cycle and fed *ad libitum* with regular Chow diet. All experiments were performed according to the DZNE internal guidelines and approved by the State Agency for Nature, Environment and Consumer Protection in North Rhine Westphalia (LANUV, NRW; application numbers: 84-02.04.2014.A521 and 81-02.04.2020.A110). In this study, we used 1-month-old *Ndufs4* KO mice (males or female) and 6-month-old *Aifm1 (R200 del)* knockin and Hq mutant males with the corresponding wt gender-matched littermates.

Postmortem human tissues

Human brain sections were obtained from The Netherlands Brain Bank (NBB), Netherlands Institute for Neuroscience, Amsterdam. All Material has been collected from donors for or from whom a written informed consent for a brain autopsy and the use of the material and clinical information for research purposes had been obtained by the NBB. The sections used in this study came from an 89-years-old female.

METHOD DETAILS

Imaging analysis and PLA quantification

PLA fluorescence-stained cells were imaged using the next generation confocal microscopes with Airyscan Zeiss LSM800 or LSM900 with a 63x oil immersion objective. All the PLA measurements were obtained using z-stacks of 5-8 images (5 images for cells *in vitro*, 8 images for cells in tissues) with a thickness of 0.5 μm between each focal plane. Images were deconvolved in ZEN blue (Zeiss) and maximum projections were obtained using Fiji/ImageJ, which was used also for the semi-automatic quantitative assessment of PLA-dots. (A) For cultured cells, images were taken with ROIs containing 6-10 cells. Single cells were cropped manually and, based on the TOM20 staining, a mitochondrial segmentation (gaussian blur filter, subtract background, auto threshold ''method=default'') was created to measure the mitochondrial area of the cell. PLA-dots were counted in the mask using the Fiji/ImageJ option ''find maxima'', excluding the possible off-target signals outside the mitochondrial network. PLA-dots were normalized based on mitochondrial area for each cell. (B) For fixed tissues, images were taken with ROIs containing 1-5 cells. Single cells were cropped and, based on cell (NeuN for CA1 neurons, calbindin for cerebellar Purkinje cells) and mitochondrial markers (TOM20), cell body and mitochondrial area were measured by applying a mask, as described above. PLA-dots were counted at single cell level, as described for the cell cultures, and normalized based on the area of the soma or mitochondria. PLA Brightfield images were obtained using an episcope apotome microscope with a 20x air objective. PLA-dots were counted in Fiji/ImageJ after the following post-processing ''inverting colors'', ''gaussian blur filter'', ''subtract background'' using the ''find maxima'' tool.

Native polyacrylamide gel electrophoresis, SDS gel electrophoresis and western blot analysis

To assess mitochondrial respiratory supercomplexes, 15 mg of brain tissues were homogenized in the presence of 200 mL of ice-cold isolation buffer, and subsequently centrifuged at 600 g for 10 min at 4°C. Coomassie staining gels were carried out using pellets

form 150 mg of proteins previously centrifuged at 7.000 g for 10 min at 4°C. Pellets were solubilized with 20 mL of sample buffer cocktail (sample buffer 4x, 5% digitonin in water), keeping a digitonin/protein ratio of 4:1. Solubilized pellets were incubated for 20 min on ice and immediately centrifuged at 20.000 g for 10 min at 4°C. Supernatants were transferred to new tubes and 1 mL of Coomassie G-250 sample additive was added to samples before loading into 3%–12% pre-casted gels. Gel electrophoresis was run at 150 V for 30 min, followed by 150 min at 250 V. Gels were fixed for 10 min with a solution containing 50% methanol and 10% acetic acid and then stained with a NOVEX Colloidal blue staining kit (Invitrogen) over night. After several washing steps with water, gels were imaged using a ChemiDoc Imager (Bio-Rad). In parallel, 100 mg of proteins were processed as described above, then transferred to a 0.2 mm PVDF membrane using a Trans-Blot Turbo Transfer System (Bio-Rad) for 11 min at 1.3 A and 25 V. Membranes were incubated 1 h with blocking solutions, then they were incubated with primary antibodies overnight at 4°C. The next day membranes were incubated with appropriate HRP-conjugated secondary antibodies for 1 h at room temperature and immunoblots were developed using ChemiDoc Imager (Bio-Rad).

For SDS gel electrophoresis, cells and/or tissues were lysed and sonicated in ice-cold RIPA buffer (SIGMA) supplemented with protease and phosphatase inhibitors (Roche). Proteins were resolved on a 10%–12% acrylamide gel and transferred onto nitrocellulose membranes (Bio-Rad). Membranes were blocked for 1 h, incubated with primary antibodies overnight at 4°C, washed and incubated with appropriate HRP-conjugated secondary antibodies for 1 h at room temperature. Immunoblots were developed with the Chemidoc imaging system (Bio-Rad) and densitometry was measured by ImageLab software (Bio-Rad).

Oxygen consumption rate measurements

Assessment of the oxygen consumption rate (OCR) in mouse brain tissue was performed as previously described (Fried et al., 2014), with slight modifications. Briefly, acute brain sections were prepared from transgenic and control mouse littermates. Animals were briefly anesthetized with Isoflurane and then sacrificed by cervical dislocation. Brains were rapidly removed and placed into pre-warmed artificial cerebrospinal fluid (aCSF: 120 mM NaCl, 3.5 mM KCl, 1.3 mM $CaCl_2$, 1 mM $MgCl_2$, 0.4 mM KH_2PO_4, and 5 mM HEPES with freshly added 10 mM glucose). Then, brains were sliced into 1 mm thick sections using a rodent brain slicer (Zivic Instruments, Pittsburgh, USA). Sections were kept in pre-warmed aCSF throughout the entire experimental procedure. A 5 mL pipette tip was then used to obtain consistent tissue punches from the cortex and cerebellum. Samples were loaded onto an XF Islet Capture Microplate (101122-100, Agilent Seahorse) and secured in the center of the well with mesh capture screens. Pre-warmed aCSF-medium (700 μl aCSF, supplemented with 4 mg/ml BSA) was immediately pipetted into each well. The microplate was then incubated at 37°C for 1 h in a CO_2-free incubator to allow for temperature and pH equilibration. The OCR was then measured with an XF24 Extracellular Flux Analyzer via the XF Cell Mito Stress Kit (Agilent Seahorse). Following 5 measurements of basal OCR, the ATP synthase inhibitor oligomycin (2 μM) as well as the mitochondrial uncoupler carbonyl cyanide 4-(trifluoromethoxy)-phenylhydrazone (FCCP, 2 μM) and the complex I/II inhibitor mix rotenone/antimycin A (0.5 μM) were successively added.

Cultured cells were seeded on cell culture microplates in culture medium 24 h before the assay. On the day of the experiment, growth media were replaced with Seahorse XF base medium supplemented with 1 mM pyruvate, 10 mM glucose, and 2 mM glutamine. Before the measurement, cells were equilibrated for 60 min in a CO_2-free incubator at 37 oC. Following three baseline measurements, oligomycin, FCCP and rotenone/antimycin A were successively added. The following concentrations were used: HAP1 cells: 1 μM oligomycin, 0.5 μM FCCP, 0.5 μM rotenone/antimycin A; iPSCs: 0.5 μM oligomycin, 1 μM FCCP, 0.5 μM rotenone/antimycin A; smNPCs: 1 μM oligomycin, 1 μM FCCP, 0.5 μM rotenone/antimycin A. At the end of the OCR assessment, cells were collected and lysed in RIPA buffer (SIGMA), supplemented with protease and phosphatase inhibitors (Roche). Protein concentrations were determined via Bradford assay. OCR values were then normalized to the respective protein contents.

Proximity ligation assay (PLA) fluorescence

Cells were washed once in PBS, fixed with 4% PFA for 5 min at 4°C, rinsed 3x 5 min with PBS. Fixed cells were permeabilized with 0.25% Triton in PBS for 1h at RT, rinsed 2x 5 min with PBS and treated with H_2O_2 (3% in dmH_2O, 50 μl/coverslip) for 30 min at RT. Cells seeded on glass coverslips were washed 2x 5 min with PBS and incubated with 50 μl Blocking Solution for 1 h at 37°C. Samples were incubated with primary antibodies (MTCO1 1:200 and NDUFB8 1:100, diluted in antibody diluent, 50 μl/coverslip) in a humidity chamber overnight at 4°C, washed 2x 5 min with pre-warmed PLA wash buffer A and finally incubated with PLA Probes 5x (in antibody diluent, 50 μl/coverslip) for 1 h at 37°C. After 2x 5 min washing with Wash buffer A, ligation reaction was carried out by incubating with the Ligation-Ligase solution (in mqH_2O, 50 μl/sample) for 1 h at 37°C. Amplification reaction was performed after 2x 2 min with PLA Wash buffer A, by incubating with the Amplification-Polymerase solution (in mqH_2O, 50 μl/sample) for 2 h at 37°C.

Brain slices were washed once in PBS while agitating, incubated with citrate buffer (pH 6.0) for 30 min at 90°C, then for another 30 min at RT. Tissues were washed 2x 5 min in PBS, permeabilized in a solution containing 0.5% Triton X-100 (in PBS) and 3% H_2O_2 (in mqH_2O, 1 mL/well) for 30 min at RT, washed 2x 5 min with PBS and incubated with Blocking Solution (50 μl/section) for 1 h at 37°C. Samples were incubated with primary antibodies as described above for 48h at 4°C, washed 2x 5 min with PLA Wash buffer A while agitating, then incubated with PLA Probes 5x (in antibody diluent, 50 μl/section) for 24 h at 4°C. After 2x 5 min washing with Wash buffer A, ligation and amplification reactions and development were performed as described above. Cells and brain sections were washed 2x 5 min with PLA Wash buffer B, incubated overnight at 4°C with the primary antibodies for mitochondria (i.e, TOM20) and cell identity (i.e., NeuN or calbindin) in blocking solution, washed 2x 5 min with PBS 1x and exposed to secondary antibodies for 2 h at RT in the dark. After 2x 5 min washing with 1x PBS, cells and brain sections were incubated with

DAPI (1:10.000 in PBS) for 10 min and 30 min at RT in the dark, respectively. Cells-seeded coverslips and brain sections were washed 3x 5 min with PBS and mounted on glass slides using Dako fluorescence Mounting medium. Samples were kept in the dark at 4°C and imaging analysis were run within 48 h.

Proximity ligation assay (PLA) brightfield

(A) Brain slices were washed once in PBS while agitating, incubated with citrate buffer (pH 6.0) for 30 min at 90°C, then for another 30 min at RT. Tissues were washed 2x 5 min in PBS, permeabilized in a solution containing 0.5% Triton X-100 (in PBS) for 1 h at RT. Tissue sections were washed 5 min with PBS, permeabilized with 3% H_2O_2 (in mqH_2O, 1 mL/well) for 30 min at RT, washed 2x 5 min with PBS and incubated with Blocking Solution (60 μl) for 1 h at 37°C. Samples were incubated with primary antibodies as described above for 48 h at 4°C, washed 2x 5 min with PLA Wash buffer A while agitating, then incubated with PLA Probes 5x (in antibody diluent, 60 μl/section) for 24 h at 4°C. After 2x 5 min washing with Wash buffer A, ligation reaction was carried out by incubating with the Ligation-Ligase solution (in mqH_2O, 60 μl/sample) for 1 h at 37°C. Amplification reaction was performed after 2x 2 min with PLA Wash buffer A, by incubating with the Amplification-Polymerase solution (in mqH_2O, 60 μl/sample) for 2 h at 37°C. After 2x 5 min washing steps with PLA Wash buffer A, samples were incubated with the 5x Detection Brightfield Solution (in mqH_2O, 60 μl/ section) for 1 h at RT. After 2x 2 min washing with mqH_2O, brain sections were mounted with 0.7% gelatin. The day after, they underwent dehydration procedure consisting of 1x 5 min in 70% ethanol, 1x 5 min in 96% ethanol, 2x 2 min in 100% ethanol, 8 min Xylene and final mounting in DPX medium.

QUANTIFICATION AND STATISTICAL ANALYSIS

Data were analysed using Graph Pad Prism and are presented as mean ± SEM. The number of biological replicates is indicated in the figure legends. Statistical analysis of normal distributed data were done with two-tailed Student's *t* test, one- or two-way ANOVA with repeated measures where appropriate, as indicated in the different parts of this study. Statistical significance was defined as $^*p < 0.05$, not significant was indicated as ns.